

## High metal content of highly accreting quasars

MARZENA ŚNIEGOWSKA,<sup>1,2</sup> PAOLA MARZIANI,<sup>3</sup> BOŻENA CZERNY,<sup>2</sup> SWAYAMTRUPTA PANDA,<sup>2,1</sup>  
MARY LOLI MARTÍNEZ-ALDAMA,<sup>2</sup> ASCENSIÓN DEL OLMO,<sup>4</sup> AND MAURO D'ONOFRIO<sup>5</sup>

<sup>1</sup>*Nicolaus Copernicus Astronomical Center, Polish Academy of Sciences, Bartycka 18, 00-716 Warsaw, Poland*

<sup>2</sup>*Center for Theoretical Physics, Polish Academy of Sciences, Al. Lotników 32/46, 02-668 Warsaw, Poland*

<sup>3</sup>*Istituto Nazionale di Astrofisica (INAF), Osservatorio Astronomico di Padova, 35122 Padova, Italy*

<sup>4</sup>*Instituto de Astrofísica de Andalucía (IAA- CSIC), Glorieta de Astronomía, E-18080 Granada, Spain*

<sup>5</sup>*Dipartimento di Fisica & Astronomia, Università di Padova, Padova, Italy*

(Received; Revised; Accepted)

Submitted to

### ABSTRACT

We present an analysis of UV spectra of 13 quasars believed to belong to extreme Population A (xA) quasars, aimed at the estimation of the chemical abundances of the broad line emitting gas. Metallicity estimates for the broad line emitting gas of quasars are subject to a number of caveats, although present data suggest the possibility of an increase along the quasar main sequence along with prominence of optical FeII emission. Extreme Population A sources with the strongest FeII emission offer several advantages with respect to the quasar general population, as their optical and UV emission lines can be interpreted as the sum of a low-ionization component roughly at quasar rest frame (from virialized gas), plus a blueshifted excess (a disk wind), in different physical conditions. Specifically, in terms of ionization parameter, cloud density, metallicity and column density. Capitalizing on these results, we analyze the component at rest frame and the blueshifted one, exploiting the dependence of several intensity line ratios on metallicity  $Z$ . We find that the validity of intensity line ratios as metallicity indicators depends on the physical conditions. We apply the measured diagnostic ratios to estimate the physical properties of sources such as density, ionization, and metallicity of the gas. Our results confirm that the two regions (the low-ionization component and the blue-shifted excess) of different dynamical conditions also show different physical conditions and suggest metallicity values that are high, and probably the highest along the quasar main sequence, with  $Z \gtrsim 10Z_{\odot}$ . We found some evidence of an overabundance of Aluminium with respect to Carbon, possibly due to selective enrichment of the broad line emitting gas by supernova ejecta.

**Keywords:** quasars: emission lines — quasars: supermassive black holes — Line: profiles — quasars: NLSy1 — quasars: super Eddington

### 1. INTRODUCTION

Thanks to large public databases as the Sloan Digital Sky Survey (SDSS) catalogs, we have unrestricted access to a large wealth of astronomical data (for example, several editions of quasar catalogues, [Schneider et al. 2010](#); [Pâris et al. 2017](#), and of value-added measurements by [Shen et al. 2011](#)). SDSS spectra of high redshift quasars

( $z \gtrsim 2$ ) cover the rest frame UV spectral range. It is known since the 1970s that measurements of UV emission lines can be used to explore the physical and chemical properties of active galactic nuclei (AGN). Landmark papers provided the basic understanding of line formation processes due to photoionization (e.g., [Wills & Netzer 1979](#); [Davidson & Netzer 1979](#); [Baldwin et al. 2003](#)).

The chemical composition of the line emitting gas is an especially intriguing problem from the point of view of the evolution of cosmic structures, but also from the technical side. [Nagao et al. \(2006b\)](#) investigated BLR

metallicities using various emission-line flux ratios and claimed that the typical metallicity of the gas in that region is at least super-solar, with typical  $Z \sim 5Z_{\odot}$ . Moreover, studies of metallicity-redshift dependence (Nagao et al. 2006b; Juárez et al. 2009) show a lack of metallicity evolution up to  $z \approx 5$ . Similar results are obtained for (Nagao et al. 2006a). The highest-redshift quasars ( $z \gtrsim 5$  Bañados et al. e.g., 2016; Nardini et al. e.g., 2019) are known to show UV spectra remarkably similar to the ones observed at low-redshift, especially the ones accreting at high rate and radiating at high Eddington ratio (Diamond-Stanic et al. 2009; Plotkin et al. 2015; Sulentic et al. 2017).<sup>1</sup> Perhaps surprisingly, these sources are suspected to have high metal content in their line emitting gas, due to the consistent values of several diagnostic ratios measured in quasars with similar spectral properties at low and high  $z$  (Martínez-Aldama et al. 2018), and indicating highly super-solar metal content.

Several techniques are applied to estimate the chemical composition in Galactic nebulae (see e.g., Feibelman & Aller 1987 for planetary nebulae). Classical techniques used for HII and other nebulae (including the Narrow Line Regions, NLRs) are unfortunately not applicable to the broad line regions of quasars. Permitted and inter-combination lines are too broad to resolve fine structure components of doublets; line profiles are composites and may originate in regions that are spatially unresolved, and unresolved or only partially resolved in radial velocity as well.

However, quasar emission line profiles still offer important clues in the radial velocity domain. The shape of the profile is strongly dependent on the ionization potential of the ionic species from which the line is emitted: it is expedient to subdivide the broad lines in low- and high ionization lines (LILs and HILs). The LIL group in the spectral range under analysis (1200 Å – 2000 Å) includes the following lines: SiII $\lambda$ 1263, SiII $\lambda$ 1814, AlII $\lambda$ 1671, AlII $\lambda$ 1860, SiIII $\lambda$ 1892, CIII $\lambda$ 1909. High ionization lines are NIV $\lambda$ 1486, OIV $\lambda$ 1402, CIV $\lambda$ 1549, SiIV $\lambda$ 1397, OIII $\lambda$ 1663, and HeII $\lambda$ 1640 (for detailed discussion see Collin-Souffrin et al. 1988; Collin-Souffrin & Lasota 1988; Gaskell 2000). The AlII, SiII, and CIII lines sometimes referred to as “intermediate ionization lines:” even if they are mainly produced within the fully ionized region of the emitting gas clouds (Negrete et al. 2012), the ionization potential of their ionic species is closer to the ones of the LILs, and typically  $\lesssim 20$  eV.

The two groups of lines (HILs and LILs) do not only show different kinematic properties (Sulentic et al. 1995), but their emission is also likely to occur in fundamentally different physical conditions (Marziani et al. 2010). The HILs are characterized also by the evidence of strong blueshifted emission, very evident in CIV (e.g., Sulentic et al. 2007; Richards et al. 2011; Coatman et al. 2016). Therefore, a careful line comparison/decomposition is necessary, lest inferences may be associated with a non-existent region with inexplicable properties.

The interpretation of two line components involves a virialized region, of relatively low ionization (hereafter referred to the virialized, low-ionization BLR associated with a symmetric broad component, BC), possibly including emission from the accretion disk, and a region of higher ionization, associated with a disk wind or a clumpy outflow, a scenario first proposed by Collin-Souffrin et al. (1988, and further developed by Elvis 2000), and observationally supported by reverberation mapping (e.g., Peterson & Wandel 1999) and the apparent lack of correlation between HILs and LILs in luminous quasars (e.g., Mejía-Restrepo et al. 2016; Sulentic et al. 2017). Even if all lines were emitted by a wind (Murray et al. 1995; Murray & Chiang 1997; Proga 2007a), the conditions at the base of the textcolorwind may strongly differ from the ones downstream in the outflow.

While each UV metal line contains information related to composition (Hamann & Ferland 1992), not all of the lines listed above can be used in practice. For instance, the NV and SiII $\lambda$ 1263 lines are strongly affected by blending with Ly $\alpha$ ; other lines such as SiII $\lambda$ 1814 and NIV $\lambda$ 1486 are usually weak and require high S/N to be properly measured. The choice of diagnostic ratios used for metallicity estimates will be a compromise between S/N, easiness of deblending, and straightforwardness of physical interpretation. In practice, apart from Ly $\alpha$ , only the strongest broad features will be considered as potential metallicity estimators in this work (Sect. 3). The ratio (SiIV+OIV)/CIV has been widely used in past studies (Hamann & Ferland 1999, and references therein); this ratio is relatively easy to measure and seems to be the most stable ratio against distribution of gas densities and ionization parameter in the BLR (Nagao et al. 2006b). The ratios involving NV $\lambda$ 1240, like NV/CIV, are apparently more sensitive to ionization parameter and sensitive to the nitrogen abundance (e.g. Dietrich et al. 2003; Wang et al. 2012a). We will rediscuss the use of these ratios in the context of the xA quasar spectral properties (Sect. 5.7).

<sup>1</sup> The effect is most likely due to a bias: for a flux limited sample, the highest radiators at a given black hole mass are the ones that remain detectable at highest  $z$  (Sulentic et al. 2014).

Both physical conditions and chemical abundances vary along the quasar main sequence (see e.g., [Sulentic et al. 2000b](#); [Kuraszkiewicz et al. 2009](#); [Shen & Ho 2014](#); [Wildy et al. 2019](#); [Panda et al. 2020b](#)). Solar and even slightly subsolar values are possible toward the extreme Population B, where FeII emission is often undetectable above noise (e.g., [Hamann et al. 2002](#); [Punsly et al. 2018](#)). At the other extreme, where FeII is most prominent, estimates suggest  $Z \gtrsim 10Z_{\odot}$  ([Panda et al. 2018, 2019](#)). [Baldwin et al. \(2003\)](#) derived  $Z \approx 15Z_{\odot}$ , although in the particular case of a “nitrogen-loud” quasars. Apart from the extremes, it is not obvious whether there is a continuous systematic trend along the sequence. Previous estimates consistently suggest super-solar metallicity up to  $Z \lesssim 10 Z_{\odot}$  ([Warner et al. 2004](#)). Other landmark studies consistently found super-solar metallicity: [Hamann & Ferland \(1992\)](#) derived  $Z$  up to  $\lesssim 15Z_{\odot}$ ; [Nagao et al. \(2006b\)](#) found typical values  $Z \approx 5Z_{\odot}$ , with  $Z \sim 10Z_{\odot}$  for the most luminous quasars from the (SiIV+OIV)/CIV ratio. [Sulentic et al. \(2014\)](#) inferred a large dispersion with the largest value in excess of  $10Z_{\odot}$ . Similar results were reached by [Shin et al. \(2013\)](#) whose SiIV+OIV]/CIV ratio measurements suggested  $Z \gtrsim 10Z_{\odot}$ .

Most interesting along the quasar main sequence are the high accretors. They are selected according to empirical criteria (e.g., [Wang et al. 2013](#); [Marziani & Sulentic 2014](#); [Wang et al. 2014](#); [Du et al. 2016a](#)), and defined by having  $R_{\text{FeII}} > 1$ , that is with the FeII $\lambda$ 4570 blend on the blue side of H $\beta$  (as defined by [Boroson & Green 1992](#)) flux exceeding the flux of H $\beta$ . In the optical diagram of the quasar main sequence ([Sulentic et al. 2000b](#); [Shen & Ho 2014](#)) they are at the extreme tip in terms of FeII prominence, and identified as extreme Population A (hereafter xA), following [Sulentic et al. \(2002\)](#). Depending on redshift, we look for high accretors using different criteria. In case of  $z \gtrsim 1$ , it is expedient to use a criterion based on two UV line intensity ratios:

- $\text{AlIII}/\text{SiIII}] > 0.5$
- $\text{CIII}]/\text{SiIII}] < 1.0$ ,

following ([Marziani & Sulentic 2014](#)). These criteria are met by the sources identified as xA Population by Sulentic and collaborators. xA quasars are radiating at the highest luminosity per unit mass, and, at low  $z$  they are characterized by relatively low black hole masses for their luminosities and high Eddington ratios ([Mathur 2000](#); [Sulentic et al. 2000a](#)). There is evidence that xA sources tend to have high-metallicity ([Shemmer et al. 2004](#); [Martínez-Aldama et al. 2018](#)). Similar properties have been identified as characteristic of narrow-line

Seyfert 1 galaxies (NLSy1s) with strong FeII emission. NLS1s also have unusually high metallicities for their luminosities. [Shemmer & Netzer \(2002\)](#) have shown that NLSy1s deviate significantly from the nominal relationship between metallicity and luminosity in AGN. As several studies distinguish between NLSy1s and “broader-lined” AGN, we remark here that all FeII strong NLSy1s meeting the selection criterion  $R_{\text{FeII}} > 1$  are extreme Pop. A sources.<sup>2</sup>

The aim of this work is to investigate the metallicity-sensitive diagnostic ratios of the UV spectral range for extreme Population A quasars i.e., for highly accreting quasars. Section 2 defines the selection of our sample, and provides some basic information on the sample quasars. In Sect. 3 we define the diagnostic ratios, and describe the basic observational results. In Section 4 we compare measured diagnostic ratios and we compare them with the ones obtained from photoionization simulations. In Sect. 5 we discuss our results in terms of method caveats, metal enrichment, accretion parameters and their implications on the nature of xA sources. We show the UV spectra in Appendix A along with the multicomponent fit analysis of the emission blends, and in the Appendix B we show the trend of  $Z$ -sensitive ratios as a function of ionization parameter, density, and metallicity.

## 2. SAMPLE

### 2.1. Sample definition

Qualitatively, extreme Pop. A objects show prominent AlIII and weak or absent CIII] emission lines. In general, they show low emission line equivalent widths ( $\approx \frac{1}{2}$  of them meet the  $W(\text{CIV}) \lesssim 10 \text{ \AA}$ , and qualify as weak-lined quasars following [Diamond-Stanic et al. 2009](#)),<sup>3</sup> and a spectrum that is easily recognizable even by a visual inspection, also because of the “trapezoidal” shape of the CIV profile and the intensity of the  $\lambda 1400$  blend, comparable to the one of CIV ([Martínez-Aldama et al. 2018](#)).

xA sources were selected according to the criteria given in Sect. 1, using line measurements automatically

<sup>2</sup> NLSy1s are identified by the line width of the H $\beta$  broad component being  $\text{FWHM}(\text{H}\beta_{\text{BC}}) \leq 2000 \text{ km s}^{-1}$  ([Osterbrock & Pogge 1985](#)), Pop. A sources are identified  $\text{FWHM}(\text{H}\beta_{\text{BC}}) \leq 4000 \text{ km s}^{-1}$  ([Sulentic et al. 2000a](#)). Imposing a fixed limit on line FWHM, although very convenient observationally, has no direct physical meaning, and its interpretation might be sample dependent. See [Marziani et al. \(2018\)](#) for a discussion of the issue.

<sup>3</sup> Weak-lined quasars are mostly xA sources, judging from their location along the MS ([Marziani et al. 2016a](#)), and that the limit at  $W \approx 10 \text{ \AA}$  separates the low- $W$  side of a continuous distribution of the xA CIV equivalent width peaked right at around  $10 \text{ \AA}$  ([Martínez-Aldama et al. 2018](#)).

obtained by the `splot` task with a cursor script within the IRAF data reduction package. We focus on the spectral range from  $\approx 1200 \text{ \AA}$  to  $2100 \text{ \AA}$ , where (1) UV lines used for xA identification are present; (2) the strongest emission features helpful for metallicity diagnostics are also located. The  $\text{Ly}\alpha + \text{Nv}$  blend is usually too heavily compromised by absorptions which make it impossible to reconstruct the emission components especially for  $\text{Ly}\alpha$ . We will make some consideration on the mean strength of the Nv with respect to C IV and  $\text{HeII}\lambda 1640$  (Sect. 5.3), but will not consider Nv as a diagnostics. We selected SDSS DR12<sup>4</sup> spectra in the redshift range  $2.15 < z < 2.40$ , relatively bright ( $r < 19$ ) to ensure moderate-to-high S/N in the continua (in all cases  $S/N \gtrsim 5$  in the continuum, and the wide majority with  $S/N \gtrsim 10$ ), and of low declination  $\delta < 10$ . The redshift range was chosen to allow for the possibility of  $H\beta$  coverage in the  $H$  band by eventual near-IR spectroscopic observations. The DR12 sample selected with these criteria is  $\approx 500$  sources strong. xA sources were selected out of this sample with an automated procedure, inspected to avoid broad absorption lines, and further vetted for obtained a small pilot sample of  $\sim 10$  sources. A larger sample of xA sources will be considered in a subsequent work (Garnica et al., in preparation). The final selection includes 13 sources. With the adopted selection criteria in flux and redshift, we expect a small dispersion in the accretion parameters (especially luminosity; Sect. 5.2). Indeed, the selected sources are rather homogeneous in terms of spectral appearance, with a few sources included in our sample that however show borderline criteria. They will be considered in Sect. 4.1.1 in terms of their individual  $U$ ,  $n_H$ .

## 2.2. Sample properties

Table 1 provides basic information for the 13 sources of our sample: SDSS name, redshift from the SDSS, the difference between our redshift estimation using AlIII (described in 3.1) and the SDSS redshift  $\delta z = z - z_{\text{SDSS}}$ , the  $g$ -band magnitude provided by Adelman-McCarthy et al. (2008a), the  $g - r$  color index, the rest-frame-specific continuum flux at  $1700 \text{ \AA}$  and  $1350 \text{ \AA}$  measured on the rest frame, the S/N at  $1450 \text{ \AA}$ . All other sources were covered by the FIRST (Becker et al. 1995), but undetected. Considering that the typical rms scatter of FIRST radio maps is  $\approx 0.15 \text{ Jy}$ , and the typical fluxes of in the  $g$  band, we have upper limits  $\lesssim 5$  in the radio-to-optical ratio, qualifying the sample sources as radio quiet. Distances were computed using the formula

provided by Sulentic et al. (2006, their Eq. B.5), and  $\Lambda$ CDM cosmology ( $\Omega_\Lambda = 0.7, \Omega_M = 0.3, H_0 = 70 \text{ km s}^{-1} \text{ Mpc}^{-1}$ ). The bolometric luminosity is around  $\sim 10^{47} \text{ erg s}^{-1}$ , assuming a bolometric correction  $\text{B.C.}_{1350} = 3.5$  (Richards et al. 2006). The sample rms is just  $\approx 0.2 \text{ dex}$ : all sources are in a narrow range of distances and have observed fluxes within a factor  $\approx 2$  from their average. This is, in principle, an advantage for the estimation of the physical parameters such as  $L/L_{\text{Edd}}$ , considering the large uncertainty and serious biases associated with the estimation of  $M_{\text{BH}}$  from UV high-ionization lines. Accretion parameters will be discussed in Sect. 5.2.

## 3. METHODS

### 3.1. Redshift determination

The estimate of the quasar systemic redshift in the UV is not trivial, as there are no low-ionization narrow lines available in the spectral range (Vanden Berk et al. 2001). In practice, one can resort to the broad LIL. Negrete et al. (2014) and Martínez-Aldama et al. (2018) consider the  $\text{SiII}\lambda 1263$  and  $\text{OII}\lambda 1302$  lines to obtain a first estimate. A re-adjustment is then made from the wavelength of the AlIII doublet which is found, in almost all cases, to have a consistent redshift. To determine the AlIII shift those authors used multicomponent fits with all the lines in the region of the blend  $\lambda 1900$  included. The peak of AlIII is clearly visible in the spectra of our sample, since in high accretors emission of AlIII is strong with respect to the other lines in the blend at  $\lambda 1900 \text{ \AA}$ . We decided to use only this method for redshift estimation (in Tab. 1) and to measure the peak we use single Gaussian fitting from the `splot` task of the AlIII doublet and/or of the  $\text{SiIII}]$  line, depending on which feature is sharper. The obtained values are usually  $\geq z_{\text{SDSS}}$  (Table 1). This is not a surprise as  $z_{\text{SDSS}}$  is based on lines that are mainly blueshifted in xA sources, and hence is a systematic underestimation of the unbiased redshift.

### 3.2. Diagnostic ratios sensitive to $U$ , density, $Z$

Line ratios are sensitive to different parameters. In the UV range, three groups of diagnostic ratios are defined in the literature (e.g. Negrete et al. 2012; Martínez-Aldama et al. 2018).

- $\text{CIV}/[\text{SiIV}+\text{OIV}]$ ,  $\text{CIV}/\text{HeII}$  have been widely applied as metallicity indicators (e.g., Shin et al. 2013). In principle,  $\text{CIV}/\text{HeII}$  and  $\text{SiIV}/\text{HeII}$  should be sensitive to C and Si abundance because the He abundance can be considered constant. The ionization potentials of  $\text{C}^{2+}$  and  $\text{He}^+$  are similar. The main difference is that the HeII line is a recombination line, equivalent to  $\text{H I H}\alpha$ ,

<sup>4</sup> <https://www.sdss.org/dr12/>



**Table 1.** Source identification and basic properties

SDSS NAME	$z_{\text{SDSS}}$	$\delta z$	$g$	$g - r$	$f_{\lambda}(1700 \text{ \AA})$	$f_{\lambda}(1350 \text{ \AA})$	S/N
(1)	(2)	(3)	(4)	(5)	(6)	(7)	(8)
J010657.94-085500.1	2.355	0.006	18.18	0.095	662	951	20
J082936.30+080140.6	2.189	0.008	18.366	0.302	672	939	11
J084525.84+072222.3	2.269	0.017	18.204	0.331	668	989	13
J084719.12+094323.4	2.295	0.004	18.940	0.234	368	511	17
J085856.00+015219.4	2.160	0.002	17.916	0.255	709	1204	21
J092641.41+013506.6	2.181	0.004	18.591	0.337	377	670	21
J094637.83-012411.5	2.212	0.002	18.561	0.178	385	595	18
J102421.32+024520.2	2.319	0.008	18.49	0.177	478	694	23
J102606.67+011459.0	2.253	0.003	18.982	0.206	428	525	13
J114557.84+080029.0	2.338	0.009	18.545	0.369	243	360	5
J150959.16+074450.1	2.255	0.008	18.938	0.278	223	346	9
J151929.45+072328.7	2.394	0.008	18.662	0.171	405	507	19
J211651.48+044123.7	2.352	0.000	18.825	0.220	404	573	32

NOTE—Columns are as follows: (1) SDSS coordinate name; (2) SDSS redshift; (3) correction to redshift estimated in the present work ( $\delta z = z - z_{\text{SDSS}}$ ); (4)  $g$ -band magnitude from [Adelman-McCarthy et al. \(2008b\)](#); (5) color index  $g - r$ ; (6) continuum flux measured at 1700 Å in units of  $10^{-17} \text{ erg s}^{-1} \text{ cm}^{-2} \text{ \AA}^{-1}$ ; (7) continuum flux measured at 1350 Å in the same units; (8) S/N measured at continuum level at 1450 Å.

and the regions where they are formed are not co-incident (see Fig. 4).

- Ratios involving Nv, Nv/Civ and Nv/HeII have been also widely used in past work, after it was noted that the Nv line was stronger than expected in a photoionization scenario (e.g., [Osmer & Smith 1976](#)). A selective enhancement of nitrogen ([Shields 1976](#)) is expected due to secondary production of N by massive and intermediate mass stars, yielding  $[\text{N}/\text{H}] \propto Z^2$  ([Vila-Costas & Edmunds 1993](#); [Izotov & Thuan 1999](#)). This process might be especially important at the high metallicities inferred for the quasar BLR. Therefore estimates based on Nv may differ in a systematic way from estimates based on other metal lines (e.g., [Matsuoka et al. 2011](#)). In the present sample of quasars, contamination by narrow and semi-broad absorption is severe, and even if we model precisely the high ionization lines, it might be impossible to reconstruct the unabsorbed profile of the red wing of Ly $\alpha$ . In addition, S/N is not sufficient to allow for a careful measurement of NIV] $\lambda$ 1486 and NIII] $\lambda$ 1750 lines. We defer the systematic analysis of nitrogen lines to a subsequent work, while discussing the consistency of the Nv measures in a high- $Z$  scenario (Sect. 5.3).
- The ratios AlIII/SiIII] and SiIII]/CIII] are sensitive to density, as the ratios involve intercombination lines with a well defined critical density ( $n_c \sim 10^9$

$\text{cm}^{-3}$  for CIII] ([Hamann et al. 2002](#)) and  $n_c \sim 10^{11} \text{ cm}^{-3}$  for AlIII and SiIII] ([Negrete et al. 2010](#))).

- SiIII]/SiIV, SiII $\lambda$ 1814/SiIII], and SiII $\lambda$ 1814/SiIV are sensitive to the ionization parameters and insensitive to  $Z$ , as they are different ionic species of the same element.

Other intensity ratios entail a dependence on metallicity  $Z$ , but also on ionization parameter  $U$  and density  $n_{\text{H}}$ .

### 3.3. Line interpretation and diagnostic ratios

The comparison between LILs and HILs has provided insightful information over a broad range of redshift and luminosity ([Corbin & Boroson 1996](#); [Marziani et al. 1996, 2010](#); [Sulentic et al. 2017](#); [Bisogni et al. 2017](#); [Shen 2016](#); [Vietri et al. 2018](#)). A LIL-BLR appears to remain basically virialized ([Marziani et al. 2009](#); [Sulentic et al. 2017](#)), as the H $\beta$  profile remains (almost) symmetric and unshifted with respect to rest frame even if CIV blueshifts can reach several thousands of  $\text{km s}^{-1}$ . In Population A, the lines have been decomposed into two components:

- The broad component (BC), also known as the intermediate component, the core component or the central broad component following various authors (e.g., [Brotherton et al. 1994](#); [Popović et al. 2002](#); [Kovačević-Dojčinović & Popović 2015](#); [Adhikari et al. 2016](#)). The BC is modeled by a symmetric and unshifted profile (Lorentzian for Pop.

A; Véron-Cetty et al. 2001; Sulentic et al. 2002; Zhou et al. 2006), and is believed to be associated with a virialized BLR subsystem.

- The blue shifted component (BLUE). A strong blue excess in Pop. A CIV profiles is obvious, as in some CIV profiles – like the one of the xA prototype I Zw1 or high luminosity quasars – BLUE dominates the total emission line flux (Marziani et al. 1996; Leighly & Moore 2004; Sulentic et al. 2017). For BLUE, there is no evidence of a regular profile, and the fit attempts to empirically reproduce the observed excess emission. BLUE is detected in a LIL such as H $\beta$  at a very low level, and is not strongly affecting FWHM measurements (Negrete et al. 2018).

### 3.3.1. Broad component

Diagnostic ratios are not equally well measurable for the BC and the BLUE. For the BC, the following constraints and caveats apply:

CIV/, SiIV/, AlIII/ over HeII—HeII is weak but measurable in most of the objects. Ratios such as CIV/HeII $\lambda$ 1640, SiIV/HeII $\lambda$ 1640, AlIII/HeII $\lambda$ 1640 ( $U$ -dependent) offer  $Z$  indicators, although, as mentioned, we have to consider that the metal line formation zones are not always coincident with the one of HeII $\lambda$ 1640 (see Figure 4). Especially for the low-ionization conditions of the BC emitting gas, these ratios are well-behaved (Sect. 3.5 and 3.6) and will form the basis of the  $Z$  estimates presented in this paper.

SiIV/CIV—There are problems in estimating the SiIV line intensity: an overestimation might be possible because of difficult continuum placement (see, for example, the case of SDSSJ085856.00+015219.4 in Appendix A). The relative contribution of SiIV to the blend at  $\lambda$ 1400 is unclear (Wills & Netzer 1979). A strong BC contribution of OIV] is unlikely, as this line has a critical density  $n_c \sim 10^{10} \text{ cm}^{-3}$  (Zheng 1988, see also the isophotal contour of SiIV/OIV] in Appendix B). Our measurements are nonetheless compared to SiIV+ total OIV CLOUDY prediction.

AlIII/SiIII—This ratio is sensitive to density in the low-ionization BLR domain (Negrete et al. 2012). Values AlIII/SiIII  $> 1$  are possible if density is higher than  $10^{11} \text{ cm}^{-3}$ , the critical density of SiIII]. We will not use this parameter as a metallicity estimator, although, in principle, for fixed physical conditions (setting  $n_H$  and  $U$ ) the AlIII/SiIII] and SiIII]/CIII] ratios may become dependent mainly on electron temperature and so on metallicity (Sect. 3.5). The ratio of the total emission

in the 1900 blend AlIII+SiIII] + CIII] over CIV has been used as a metallicity estimator (Sulentic et al. 2014). Considering the uncertain contribution of FeIII emission and especially of the FeIII  $\lambda$ 1914 line in the xA spectra, we will not use the total intensity of the  $\lambda$ 1900 blend as a diagnostic.

CIV/AlIII—Biases might be associated with the estimate of the CIV $\lambda$ 1549<sub>BC</sub> especially when BLUE is so prominent that CIV $\lambda$ 1549<sub>BC</sub> contributes to a minority fraction.

### 3.3.2. BLUE component

CIV/HeII $\lambda$ 1640—The HeII $\lambda$ 1640 BLUE is well-visible merging smoothly with the red wing of CIV. The ratio CIV/HeII $\lambda$ 1640 might be affected by the decomposition of the blend, leading to an overestimate of the HeII emission. This ratio is in principle sensitive to metallicity. However, the increase is not monotonic at high  $U$  (Fig. 2). The resulting effect is that the CIV/HeII $\lambda$ 1640 ratio within the uncertainties leaves the  $Z$  unconstrained between 0.1 and 100 solar.

CIV/(OIV] + SiIV)—The blueshifted excess at  $\lambda$ 1400 is ascribed to OIV + SiIV emission. A significant contribution can be associated with OIV] and several transitions of OIV that are computed by CLOUDY (see e.g., Keenan et al. 2002) are especially relevant at high  $U$  values and moderately low  $n_H$  ( $\sim 10^8 \text{ cm}^{-3}$ ). The blue side of the line is relatively straightforward to measure for computing CIV/ $\lambda$ 1400 with a multicomponent fit, although difficult continuum placement, narrow absorption lines, and blending on the blue side make it difficult to obtain a very precise measurement. A total  $\lambda$ 1400 BLUE emission exceeding CIV is possible if, assuming  $\log U \gtrsim 0$ ,  $\log n_H \gtrsim 9 \text{ [cm}^{-3}]$ , the metallicity value is very high  $20 \lesssim Z \lesssim 100 Z_\odot$ , (Sect. 3.6).

(OIV]+SiIV)/HeII $\lambda$ 1640—By the same token, the HeII $\lambda$ 1640 overestimation may lead to a lower (OIV]+SiIV)/HeII $\lambda$ 1640 ratio.

## 3.4. Analysis via multicomponent fits

We analyze 13 objects using the `spectfit` task from IRAF (Kriss 1994). The use of the  $\chi^2$  minimization is aimed to provide a heuristic separation between the broad component (BC) and the blue component (BLUE) of the emission lines. After redshift correction following the method described in Sect. 3.1, for each source of our sample we perform a detailed modeling using various components as described below, including computation of asymmetric errors (Sect. 3.4.1). As mentioned in Sect. 3.2, in our analysis we consider five diagnostic ratios for

the BC: C IV/ $\lambda 1400$ , C IV/He II  $\lambda 1640$ , Al III/He II  $\lambda 1640$ ,  $\lambda 1400$ /He II  $\lambda 1640$ ,  $\lambda 1400$ /Al III, and three for the BLUE: C IV/ $\lambda 1400$ , C IV/He II  $\lambda 1640$ ,  $\lambda 1400$ /He II  $\lambda 1640$ . The C IV/He II  $\lambda 1640$  is used with care, as it may yield poor constraints. In addition, it is important to stress that, of the five ratios measured on the BC, only three (the ones dividing by the intensity of He II  $\lambda 1640$  BC) are independent. We compare the fit results with arrays of CLOUDY (Ferland et al. 2013) simulations for various metallicities and physical conditions (Sect. 3.5).

For each source we perform the multicomponent fitting in three ranges described below. The best fit is identified by the model with the lowest  $\chi^2$  i.e., with minimized difference between the observed and the model spectrum. Following the data analysis by Negrete et al. (2012), we use the following components:

*The continuum* —was modeled as a power-law, and we use the line-free windows around 1300 and 1700 Å (two small ranges where there are no strong emission lines) to scale it. If needed, we divide the continuum into three parts (corresponding to the three regions mentioned below). Assumed continua are shown in the Figures of Appendix A.

*Fe II emission* —usually does not contribute significantly in the studied spectral ranges. We consider the Fe II template which is based on CLOUDY simulations of Brühweiler & Verner (2008) when necessary. In practice the contamination by the blended Fe II emission yielding a pseudo-continuum is negligible. Some Fe II emission lines were detectable in only a few objects and around  $\approx 1715$  Å, at 1785 Å, and at 2020 Å. In these cases, we model them using single Gaussians.

*Fe III emission* —affects more the 1900 Å region and seems to be strong when Al III  $\lambda 1860$  is strong as well (Hartig & Baldwin 1986). To model these lines we use the template of Vestergaard & Wilkes (2001).

*Region 1300 - 1450 Å* —is dominated by the Si IV + O IV] high ionization blend with strong blueshifted component. The fainter lines as Si II  $\lambda 1306$ , O I  $\lambda 1304$  and C II  $\lambda 1335$  are also detectable. For the broad and blueshifted components we use the same model as in case of C IV and He II  $\lambda 1640$ . This spectral range is often strongly affected by absorption.

*Region 1450 - 1700 Å* —is dominated by C IV emission line which we model as a fixed in the rest-frame wavelength Lorentzian profile representing the BC and two blueshifted asymmetric Gaussian profiles vary freely. The same model is used for He II  $\lambda 1640$ .

*Region 1700 - 2200 Å* —is dominated by Al III, Si III] and Fe III intermediate - ionization lines. We model Al III and Si III] using Lorentzian profiles, following Negrete et al. (2012). C III] emission is also included in the fit, although the dominant contribution around  $\lambda 1900$  is to be ascribed to Fe III (Martínez-Aldama et al. 2018, and references therein). We use the template of Vestergaard & Wilkes (2001) to model Fe III emission. No BLUE is ascribed to these intermediate ionization lines.

*Absorption lines* —are modeled by Gaussians, and included whenever necessary to obtain a good fit.

The fits to the observed spectral ranges are shown in the Figures of Appendix A.

#### 3.4.1. Error estimation on line fluxes

The choice of the continuum placement is the main source of uncertainty in the measurement of the emission line intensities. The fits in Appendix A show that, in the majority of cases, the FWHM of the Al III and Si III] lines (assumed equal) satisfy the condition  $\text{FWHM}(\text{Al III}) \sim \text{FWHM}(\text{C IV}_{\text{BC}} \sim \text{FWHM}(\text{Si IV}_{\text{BC}})$ . Figure 1 shows the best fit, maximum and minimum placement of the continuum, which we choose empirically. With this approach the continua of Figure 1 should provide the continuum uncertainty at a  $\pm 3\sigma$  confidence.

The continuum placement strongly affects the measurement of an extended feature such as the Fe III blends and the He II  $\lambda 1640$  emission. Figure 1 makes it evident that errors on fluxes are asymmetric. The thick line shows the continuum best fit, and the thinner the minimum and maximum plausible continua. Even if the minimum and maximum are displaced by the same difference in the intensity with respect to the best fit continuum, assuming the minimum continuum would yield an increase in line flux larger than the flux decrease assuming the maximum continuum level. In other words, a symmetric uncertainty in the continuum specific flux translates into an asymmetric uncertainty in the line fluxes. To manage asymmetric uncertainties, we assume that the distribution of errors follows the triangular distribution (D' Agostini 2003). This method assumes linear decreasing in either side of maximum of the distribution (which is the best fit in our case) to the values obtained for maximum and minimum contributions of the continuum. We motivate using the triangular error distribution as a relatively easy analytical method to deal with asymmetric errors. For each line measurement we calculate the variance using the following formula for the triangular distribution:

$$\sigma^2(X) = \frac{\Delta^2 x_+ + \Delta^2 x_- + \Delta x_+ + \Delta x_-}{18} \quad (1)$$

where  $\Delta x_+$  and  $\Delta x_-$  are differences between measurement with maximum and best continuum and with best and minimum continuum respectively. To analyze error of diagnostic ratios we propagate uncertainties using standard formulas of error propagation.

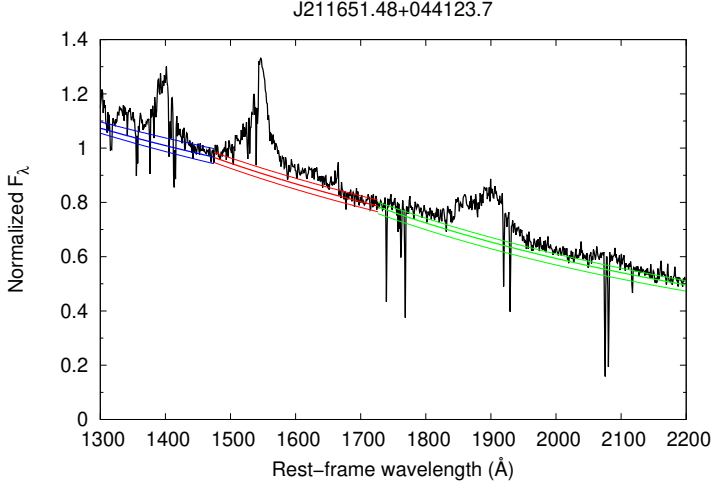


**Figure 1.** Continuum estimation for J211651.48+044123.7 from our sample. Range 1300 - 1450 Å is shown in blue, 1450 - 1700 Å in red and 1750 - 2200 Å in green. The continuum lines in each range represent from the top: the maximum, the best and the minimum continuum placement.

### 3.5. Photoionization modeling

To interpret our fitting results we compare the line intensity ratios for BC and BLUE with the ones predicted by CLOUDY simulations (Ferland et al. 2013).<sup>5</sup> An array of simulations is used as reference for comparison with the observed line intensity ratios. It was computed under the assumption that (1) column density is  $N_c = 10^{23} \text{ cm}^{-2}$ ; (2) the continuum is represented by the model continuum of Mathews & Ferland (1987) which is believed to be appropriate for Population A quasars, and (3) microturbulence is negligible. The simulation arrays cover the hydrogen density range  $7.00 \leq \log(n_H) \leq 14.00$  and the ionization parameter  $-4.5 \leq \log(U) \leq 1.00$ , in intervals of 0.25 dex. They are repeated for values of metallicities in a range encompassing five orders of magnitude: 0.01, 0.1, 1, 2, 5, 10, 20, 50, 100, 200, 500 and 1000  $Z_\odot$ . Extremely high metallicity  $Z \gtrsim 100Z_\odot$  is considered physically unrealistic ( $Z \approx 100Z_\odot$  implies that more than half of the gas mass is made up by metals!), unless the enrichment is provided in situ within

the disk (Cantiello et al. 2020). In several cases, simulations suffered convergence problems if  $Z \gtrsim 500Z_\odot$ . The behavior of diagnostic line ratios as a function of  $U$  and  $n_H$  for selected values of  $Z$  is shown in Fig. 18 of Appendix B.

#### 3.5.1. Basic Interpretation

The line emissivity  $\epsilon_{\text{coll}}$  ( $\text{ergs cm}^{-3} \text{ s}^{-1}$ ) of a collisionally excited line emitted from an element  $X$  in its  $i$ -th ionization stage has a strong temperature dependence. In the high density limit

$$\epsilon_{X^i, \text{coll}} = n_{X^i, l} \beta A_{X^i, ul} h\nu_0 \frac{g_{X^i, l}}{g_{X^i, u}} \exp\left(-\frac{h\nu_0}{kT_e}\right) \quad (2)$$

$$\propto n_{X^i, l} \exp\left(-\frac{h\nu_0}{kT_e}\right)$$

the line is said to be “thermalized,” as its strength depends only on the atomic level population and not on the transition strength (Hamann & Ferland 1999).  $\beta$  is the photon escape probability and  $A_{X^i, ul}$  is the spontaneous decay coefficient. At low densities we have,

$$\epsilon_{X^i, \text{coll}} = n_{X^i, l} n_e q_{X^i, lu} h\nu_0 \propto n_{X^i}^2 T_e^{-1/2} \exp\left(-\frac{h\nu_0}{kT_e}\right) \quad (3)$$

The recombination lines considered in our analysis are  $H\beta$  and  $\text{HeII}\lambda 1640$ , for which the emissivity (with an approximate dependence of radiative recombination coefficient  $\alpha$  on electron temperature, Osterbrock & Ferland 2006) becomes:

$$\epsilon_{Y^j, \text{rec}} = n_{Y^j} n_e \alpha h\nu_0 \propto n_{Y^j}^2 T_e^{-1} \quad (4)$$

and  $n_{Y^j}$  is the number density of the parent ion.

Under these simplifying, illustrative assumption we can write:

$$\frac{\epsilon_{X^i, \text{coll}}}{\epsilon_{Y^j, \text{rec}}} \propto \left(\frac{n_{X^i}}{n_{Y^j}}\right)^2 T_e^{\frac{1}{2}} \exp\left(-\frac{h\nu_0}{kT_e}\right) \quad (5)$$

for the low-density case, and

$$\frac{\epsilon_{X^i, \text{coll}}}{\epsilon_{Y^j, \text{rec}}} \propto \frac{n_{X^i}}{n_{Y^j}^2} T_e \exp\left(-\frac{h\nu_0}{kT_e}\right) \quad (6)$$

for the high density case.

Similarly, for the ratio of two collisionally excited lines at frequencies  $\nu_0$  and  $\nu_1$ ,

$$\frac{\epsilon_{X^i, \text{coll}}}{\epsilon_{Y^j, \text{coll}}} \propto \left(\frac{n_{X^i}}{n_{Y^j}}\right)^\kappa \exp\left(-\frac{h(\nu_0 - \nu_1)}{kT_e}\right) \quad (7)$$

where  $\kappa = 1, 2$  in the high- and low-density case respectively.

<sup>5</sup> The arrays were computed over several years with CLOUDY 13.05, in large part before CLOUDY 17 became available.



Connecting the relative chemical abundance to the line emissivity ratios in the previous equation requires the reconstruction of the ionic stage distribution for each element, i.e., the computation of the ionic equilibrium, as well as the consideration of the extension of the emitting region within the gas clouds i.e., that the line emission is not cospatial, and possible differences in optical depth effects. This is achieved by the CLOUDY simulations. However, we can see that the main variable parameter for a given relative emissivity is  $T_e$ . In other words, electron temperature is the main parameter connected to metallicity. This is especially true for fixed physical condition ( $U$ ,  $n_H$ ,  $N_c = 10^{23}$ , SED given). This is most likely the case of xA sources: the spectral similarity implies that the scatter in physical properties is modest. We further investigate this issue in Sect. 4.3.

### 3.6. Explorative analysis of photoionization trends at fixed ionization parameter and density

One of the main results of previous investigations is the systematic differences in ionization between BLUE and BC (Marziani et al. 2010; Negrete et al. 2012; Sulentic et al. 2017). Previous inferences suggest very low ionization ( $U \sim 10^{-2.5}$ ), also because of the relatively low C IV/H $\beta$  ratio for the BC emitting part of the BLR, and high density. A robust lower limit to density  $n_H \sim 10^{11.5} \text{ cm}^{-3}$  has been obtained from the analysis of the Ca II triplet emission (Matsuoka et al. 2007; Panda et al. 2020a). Less constrained are the physical conditions for BLUE emission. Apart from C IV/H $\beta \gg 1$  and Ly $\alpha$ /H $\beta$  and C IV/C III] also  $\gg 1$ , little constraints exist on density and column density. This result hardly comes as a surprise considering the difference in dynamical status associated with the two components. While it is expected that the BC is emitted in a region of high column density  $\log N_c \gtrsim 23 [\text{cm}^{-2}]$ , not last because radiation forces are proportional to the inverse of  $N_c$  (Netzer & Marziani 2010). Following Netzer & Marziani (2010) we wrote the equation of motions for a gas cloud under the combined effect of gravitation and radiation forces, and showed that the acceleration term due to radiation is inversely proportional to  $N_c$  (see also Ferland et al. 2009), this high  $N_c$  region is expected to be relatively stable (at rest frame, with no sign of systematic, large shifts in Population A) and presumably devoid of low-density gas (considering the weakness of C III], Negrete et al. 2012). The same cannot be assumed for BLUE. BLUE is associated with a high radial velocity outflow, probably with the outflowing streams creating BAL features when intercepted by the line-of-sight (e.g., Elvis 2000).

Here we consider  $\log U = -2.5$ ,  $\log n_H = 12$  (-2.5, 12), and  $\log U = 0$ ,  $\log n_H = 9$  (0, 9) as representative of the low and high-ionization emitting gas. Fig. 2 illustrates the behavior of the C IV/H $\beta$ , He II $\lambda$ 1640/H $\beta$  and C IV/He II $\lambda$ 1640 in the high and low-ionization cases as a function of metallicity. The C IV intensity with respect to H $\beta$  has a steep drop around  $Z \gtrsim 1Z_\odot$ , after a steady increase for sub-solar  $Z$ . The He II $\lambda$ 1640/H $\beta$  ratio decreases steadily, with a steepening at round solar value. Physically, this behavior is due to the high value of the ionization parameter (assumed constant), while the electron temperature decreases with metallicity, implying a much lower collisional excitation rate for C IV production. The dominant effect for the He II $\lambda$ 1640 decrease is likely the “ionization competition” between C IV and He II $\lambda$ 1640 parent ionic species (Hamann & Ferland 1999). As a consequence, the ratio C IV/He II $\lambda$ 1640 has a non-monotonic behavior with a local maximum around solar metallicity. At low ionization and high density, the behavior is more regular, as the steady increase in C IV/H $\beta$  is followed by a saturation to a maximum C IV/H $\beta$ . The He II $\lambda$ 1640/H $\beta$  ratio is constant up to solar, and steadily decreases above solar, where the ionization competition with triply ionized carbon sets on. The result is a smooth, steady increase in the C IV/He II $\lambda$ 1640 ratio.

Fig. 3 shows the behavior of the other intensity ratios used as metallicity diagnostics, for BLUE and BC. Si IV+O IV]/C IV and Si IV+O IV]/He II $\lambda$ 1640 saturate above  $100 Z_\odot$ . Only around  $Z \sim 10Z_\odot$  values C IV/Si IV+O IV]  $\lesssim 1$  are possible, but the behavior is not monotonic and the ratio rises again at  $Z \gtrsim 30Z_\odot$ , with the unpleasant consequence that a ratio C IV/Si IV+O IV]  $\approx 1.6$  might imply  $10 Z_\odot$  as well as  $1000 Z_\odot$ . The ratios usable for the BC also show regular behavior. The C IV/Al III] ratio remains almost constant up  $Z \sim 0.1Z_\odot$ , and then starts a regular decrease with increasing  $Z$ , due to the decrease of  $T_e$  with  $Z$  (C IV is affected more strongly than Al III]). Interestingly, Al III]/He II $\lambda$ 1640 shows the opposite trend, due to the steady decrease of the He II $\lambda$ 1640 prominence with  $Z$ . Especially of interest is however the behavior of ratio Al III]/He II $\lambda$ 1640 that shows a monotonic, very linear behavior in the log-log diagram. As for the high-ionization case, values (Si IV+O IV])/C IV  $\gtrsim 1$  are possible only at very high metallicity, although the non-monotonic behavior (around the minimum at  $Z \approx 200Z_\odot$ ) complicates the interpretation of the observed emission line ratios.

The ionization structure within the slab remains self-similar over a wide metallicity range, with the same systematic differences between the high and low-ionization

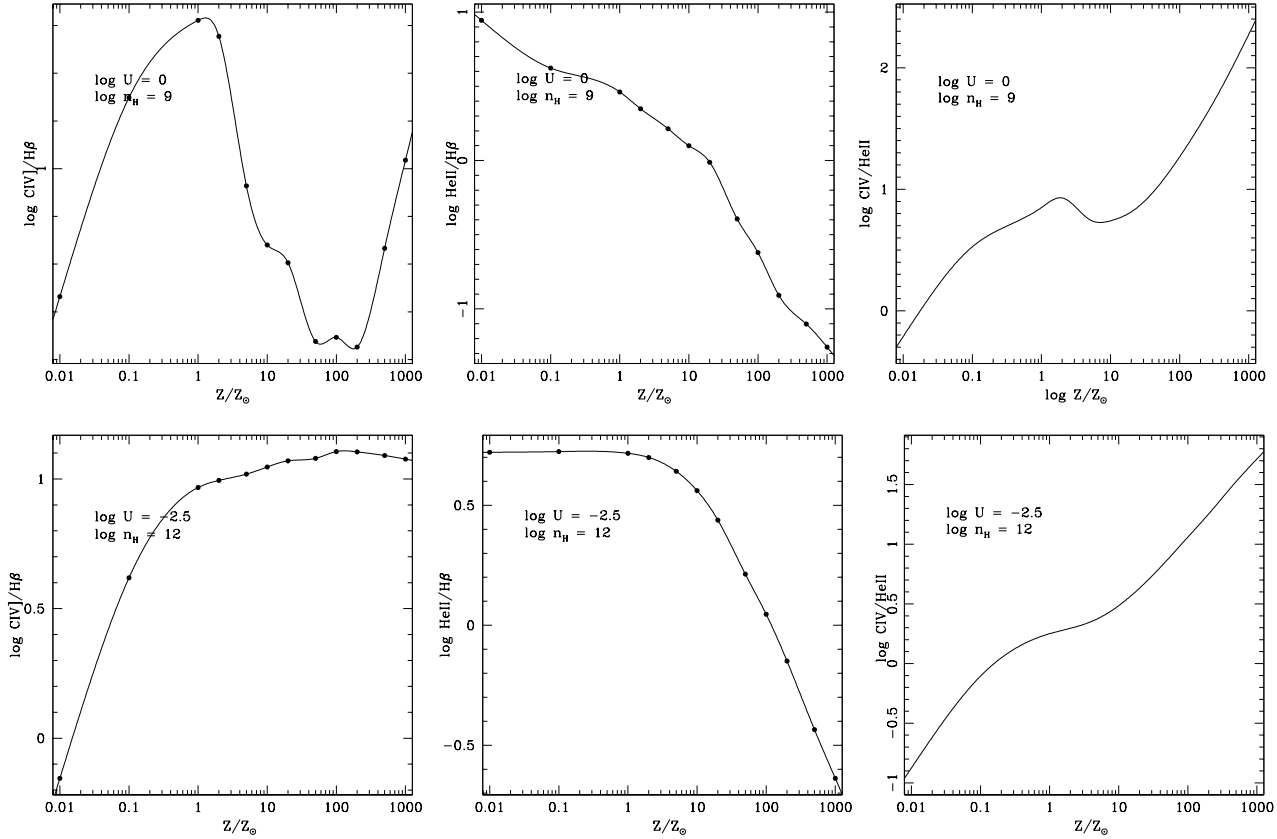


**Figure 2.** Computed intensity ratios involving CIV and HeII $\lambda$ 1640 as a function of metallicity, for physical parameters  $U$  and  $n_H$  fixed:  $(\log U, \log n_H) = (-1, 9)$  (top) and  $(\log U, \log n_H) = (-2.5, 12)$  (bottom). Columns from left to right show CIV/H $\beta$ , HeII $\lambda$ 1640/H $\beta$ , CIV/HeII $\lambda$ 1640.

case (Fig. 4), consistent with the assumption of a constant ionization parameter. As expected, the electron temperature decreases with metallicity, and the transition between the fully and partially ionized zone (FIZ and PIZ) occurs at smaller depth. In addition, close to the illuminated side of the cloud the electron temperature remains almost constant; the gas starts becoming colder before the transition from FIZ to PIZ. The depth at which  $T_e$  starts decreasing is well-defined, and its value becomes lower with increasing  $Z$  (Fig. 4). The effect is present for both the low- and high-ionization case, although it is more pronounced for the high-ionization. Fig. 5 shows that an increase in metallicity is affecting the  $T_e$  in the line emitting cloud. Fig. 5 reports the behavior of  $T_e$  at the illuminated face of the cloud ( $\tau \sim 0$ ) and at maximum  $\tau$  (corresponding to  $N_c = 10^{23} \text{ cm}^{-2}$ , the side facing the observer) for the high-ionization and low-ionization case. The  $T_e$  monotonically decreases as a function of metallicity. The difference between the two cloud faces is almost constant for the low ionization case, with  $\delta \log T_e \approx 0.5$  dex, while it increases for the

high-ionization case, reaching  $\delta \log T_e \approx 0.75$  dex at the highest  $Z$  value considered,  $10^3 Z_\odot$ .

## 4. RESULTS

### 4.1. Immediate Results

The observational results of our analysis involve the measurements of the intensity of the line BC and BLUE component separately. The rest-frame spectra with the continuum placements, and the fits to the blends of the spectra are shown in Appendix A. Table 2 reports the measurement for the  $\lambda$ 1900 blend. The columns list the SDSS identification code, the FWHM (in units of  $\text{km s}^{-1}$ ) and equivalent width and flux of AlIII (the sum of the doublet lines, in units of  $\text{\AA}$  and  $10^{-14} \text{ erg s}^{-1} \text{ cm}^{-2}$ , respectively), FWHM and flux of CIII], and flux of SiIII] (its FWHM is assumed equal to the one of the single AlIII lines.) with Similarly, Table 3 reports the parameter of the CIV blend: equivalent width, FWHM and flux of the CIV BC, the flux of the CIV blueshifted component, as well as the fluxes of the BC and BLUE of HeII $\lambda$ 1640. FWHM values are reported but especially values  $\gtrsim 5000 \text{ km s}^{-1}$  should be considered as highly uncertain. There is the concrete possibility of an ad-

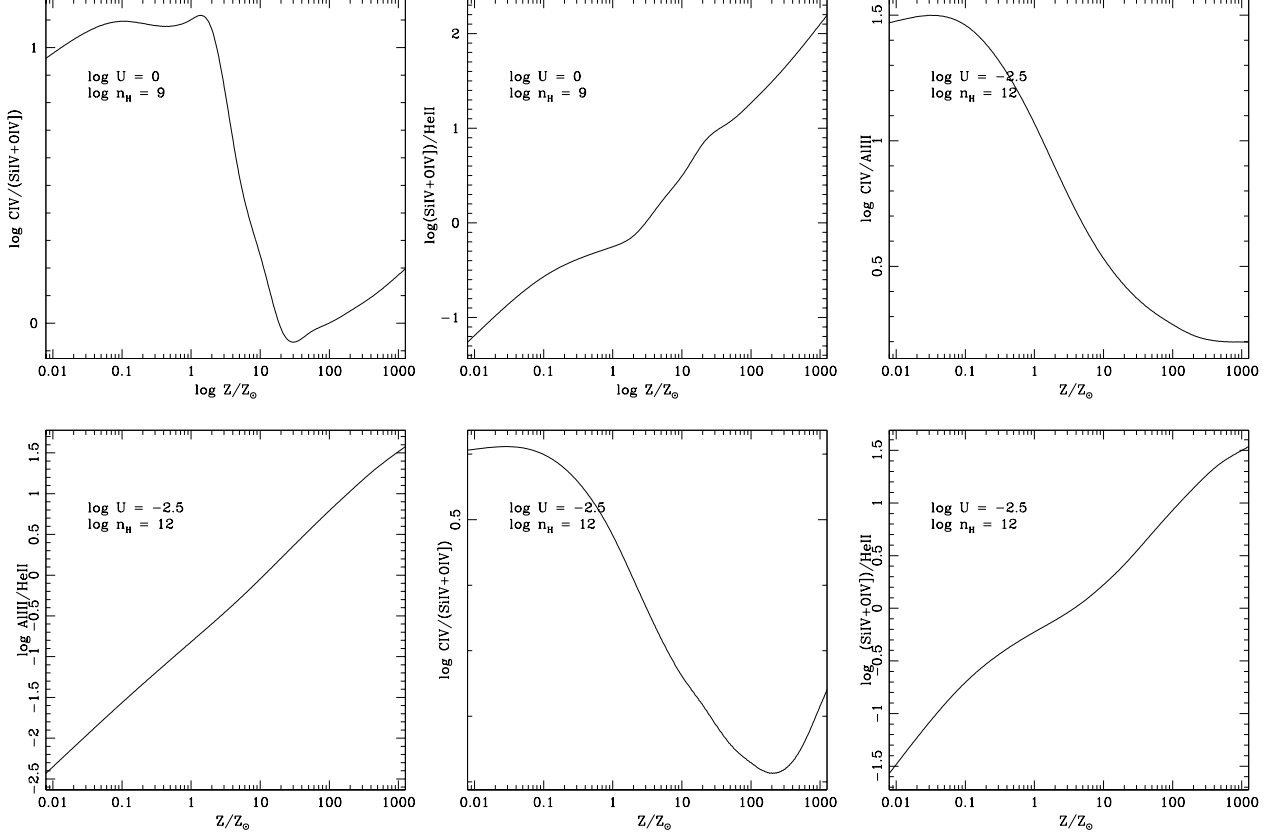


**Figure 3.** Behavior of the intensity ratios employed in this work (with the exception of  $\text{CIV}/\text{HeII}\lambda 1640$  shown in the previous Figure), as a function of metallicity, for physical parameters  $U$  and  $n_{\text{H}}$  fixed:  $(\log U, \log n_{\text{H}}) = (-1, 9)$  and  $(\log U, \log n_{\text{H}}) = (-2.5, 12)$ . Top panels, from left to right:  $\text{CIV}/\text{SiIV}+\text{OIV}$ ,  $(\text{SiIV}+\text{OIV})/\text{HeII}\lambda 1640$ ,  $\text{CIV}/\text{AlIII}$ . Bottom panes, from left to right:  $\text{AlIII}/\text{HeII}\lambda 1640$ ,  $\text{CIV}/(\text{SiIV}+\text{OIV})$ ,  $(\text{SiIV}+\text{OIV})/\text{HeII}\lambda 1640$ .

ditional broadening ( $\sim 10\%$  of the observed FWHM) associated with non-virial motions for the  $\text{AlIII}$  line (del Olmo et al., in preparation). The fluxes of the BC and of BLUE of  $\text{SiIV}$  and  $\text{OIV}$  are reported in Table 4. Intensity ratios with uncertainties are reported in Table 5. The last row lists the median values of the ratios with their semi-interquartile ranges (SIQR).

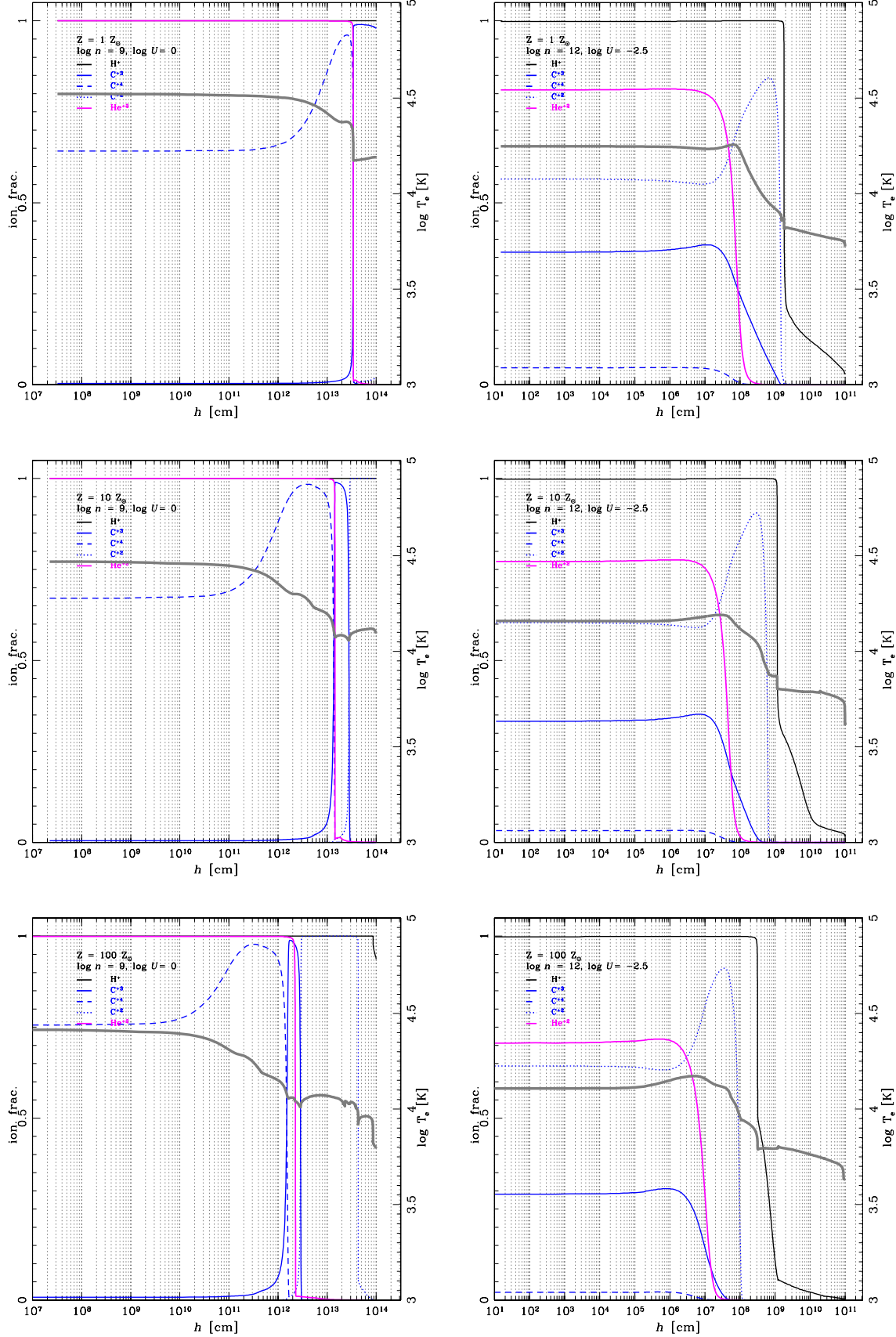
#### 4.1.1. Identification of *xA* sources and of “intruders”

Figure 6 shows that the majority of sources meet both UV selection criteria, and should be considered *xA* quasars. The median value of the  $\text{AlIII}/\text{SiIII}$  (last row of Table 5) implies that the  $\text{AlIII}$  is strong relative to  $\text{SiIII}$ . Also  $\text{SiIII}$  is stronger than  $\text{CIII}$ . Both selection criteria are satisfied by the median ratios. Only one source (SDSS J084525.84+072222.3) shows  $\text{CIII}/\text{SiIII}$  significantly larger than 1. This quasar is however confirmed as an *xA* by the very large  $\text{AlIII}/\text{SiIII}$ , by the blueshift of  $\text{CIV}$ , and by the prominent  $\lambda 1400$  blend comparable to the  $\text{CIV}$  emission. The lines in the spectrum of SDSS J084525.84+072222.3 are broad, and any  $\text{CIII}$  emis-

sion is heavily blended with  $\text{FeIII}$  emission. The  $\text{CIII}$  value should be considered an upper limit. Three outlying/borderline data points (in orange) in Fig. 6 have ratio  $\text{CIII}/\text{SiIII} \sim 1$ , and  $\text{AlIII}/\text{SiIII}$  consistent with the selection criteria within the uncertainties, but other criteria support their classification as *xA*. The borderline sources will be further discussed in Section 4.3. In conclusion, all the 13 sources of the present sample save one should be considered bona-fide *xA* sources.

It is intriguing that the intensity ratios  $\text{CIII}/\text{SiIII}$  and  $\text{AlIII}/\text{SiIII}$  are apparently anti-correlated in Figure 6, if we exclude the two outlying points. Excluding the two outlying data point the Spearman rank correlation coefficient is  $\rho \approx 0.8$ , which implies a  $4\sigma$  significance for a correlation, but the correlation coefficient between the two ratios for the full sample is much lower. Given the small number of sources, a larger sample is needed to confirm the trend.

#### 4.1.2. BC intensity ratios



**Figure 4.** Computed ionization fraction and electron temperature (thick grey line) as a function of depth within the emitting gas slab, for physical parameters  $U$  and  $n_H$  fixed:  $(\log U, \log n_H) = (-1, 9)$  (representative of BLUE and high ionization case, left) and  $(\log U, \log n_H) = (-2.5, 12)$  (representative of the low-ionization BLR, right), in order of increasing metallicity from top to bottom.



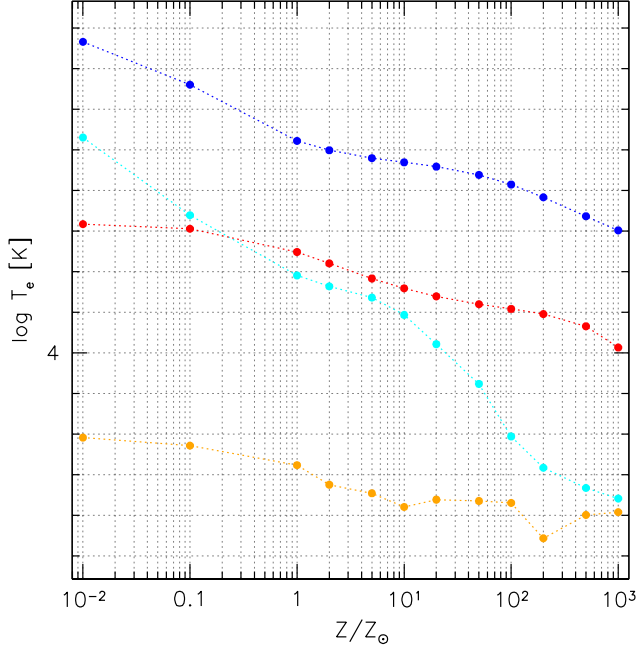


**Figure 5.** Electron temperature  $T_e$  as a function of metallicity  $Z$ , for physical parameters  $U$  and  $n_H$  fixed:  $(\log U, \log n_H) = (-1, 9)$  (representative of BLUE and high ionization case, blue and cyan) and  $(\log U, \log n_H) = (-2.5, 12)$  (representative of the low-ionization BLR, red and orange). Blue and red refer to the first zone of the CLOUDY computation i.e., to the illuminated surface of the clouds; cyan and orange, to the side of the cloud farther from the continuum sources i.e., facing the observer.

Fig. 7 shows the distribution of diagnostic intensity ratios  $CIV/HeII\lambda 1640$ ,  $SiIV/HeII\lambda 1640$ , and  $AlIII/HeII\lambda 1640$  for the BC. The lower panels of Fig. 7 shows the results for individual sources.

The vertical lines identify the median values,  $\mu_{1/2}(CIV/HeII\lambda 1640) \approx 4.03$ ,  $\mu_{1/2}(AlIII/HeII\lambda 1640) \approx 4.31$ ,  $\mu_{1/2}(SiIV/HeII\lambda 1640) \approx 6.39$ . The higher value for  $SiIV/HeII\lambda 1640$  than for  $CIV/HeII\lambda 1640$  implies  $\mu_{1/2}(CIV/SiIV) \approx 0.69$ , a value that is not predicted by any CLOUDY simulation, not even at the highest metallicity. The  $CIV/AlIII$  ratio is also out of scale: the minimum  $CIV/AlIII$  predicted by the simulations at low ionization is  $\approx 1.6$ , reached at extremely high  $Z$  ( $\sim 1000Z_\odot$ ).

However, the distribution of the data points is relatively well-behaved, with individual ratios showing small scatter around their median values. In the histogram, we see a tail made by a 4-5 objects suggesting systematically higher values. In particular, at least two objects (SDSS J102606.67+011459.0 and SDSS J085856.00+015219.4) show systematically higher ratios, with  $CIV/HeII\lambda 1640 \approx 10$ , and  $AlIII/HeII\lambda 1640 \approx 4$ .

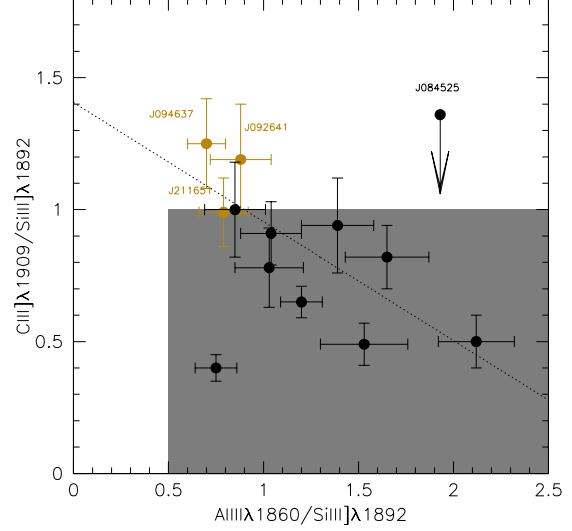


**Figure 6.** Relation between intensity ratios  $AlIII\lambda 1860/SiIII\lambda 1892$  and  $CIII\lambda 1909/SiIII\lambda 1892$ . The gray area corresponds to the parameter space occupied by the xA sources. Borderline sources are in orange color.

Both of them show extreme  $CIV$  blueshifts and SDSS J102606.67+011459.0 shows the highest  $AlIII/SiIII$  ratio in the sample.

Since the three ratios are, for fixed physical conditions, proportional to metallicity, we expect an overall consistency in their behavior i.e., if one ratio is higher than the median for one object, also the other intensity ratios should be also higher. The lower diagrams are helpful to identify sources, for which only one intensity ratio deviates significantly from the rest of the sample. A case in point is SDSS J082936.30+080140.6 whose ratio  $AlIII/HeII\lambda 1640 \approx 8$  is one of the highest values, but whose  $CIV/HeII\lambda 1640$  and  $SiIV/HeII\lambda 1640$  are slightly below the median values. The fits of Appendix A show that this object is indeed extreme in  $AlIII$  emission. The  $CIV$  and  $\lambda 1400$  blends are dominated by the BLUE excess, and an estimate of the  $CIV$  and  $SiIV$  BC is very difficult, as it accounts for a small fraction of the line emission. The  $HeII\lambda 1640$  emission is almost undetectable, especially in correspondence to the rest frame. Ideally, results on these objects should be discussed on a case-by-case basis.

#### 4.1.3. BLUE intensity ratios

Similar considerations apply to the blue intensity ratios. We see systematic trends in Figure 8 that imply consistency of the ratios for most sources, although the uncertainties are larger, especially for  $CIV/HeII\lambda 1640$ . The ratio  $CIV/(SiIV + OIV)$  values are systematically higher than for the BC, while the  $CIV/HeII\lambda 1640$  is

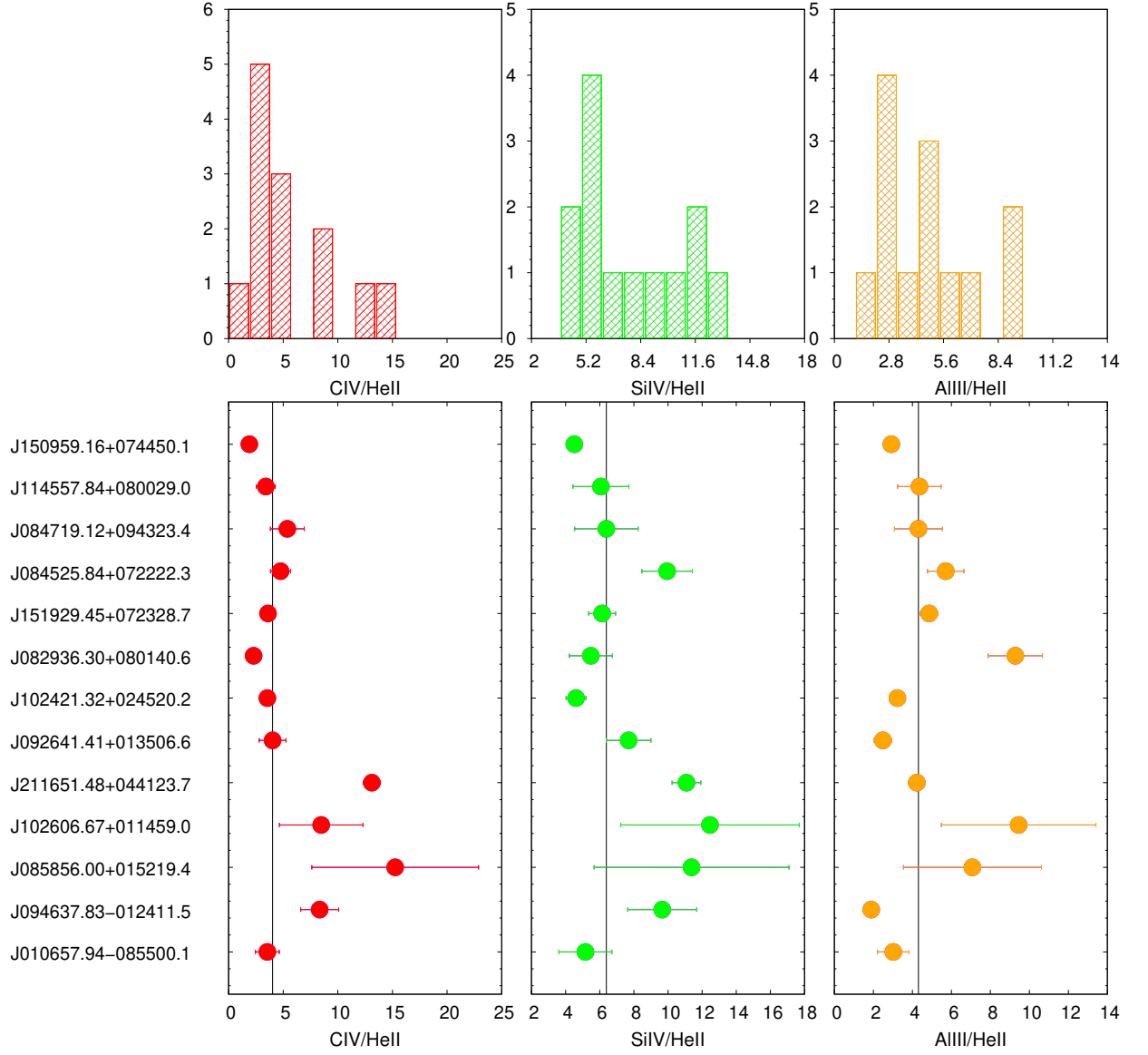


**Figure 7.** Distribution of diagnostic intensity ratios based on the BC (top) for CIV/HeII $\lambda$ 1640 (red), SiIV/HeII $\lambda$ 1640 (green) and AlIII/HeII $\lambda$ 1640 (orange). The lower panels show results and associated uncertainties for individual sources with the same color-coding as histograms. Vertical black line in lower panel represents median value of sources measurements.

slightly higher (median BLUE 5.8 vs. median BC 4.38). The ratio (SiIV + OIV)/HeII $\lambda$ 1640 is much lower than for the BC (median BLUE 2.09 vs. median BC 6.27). The difference might be in part explained by the difficulty of deblending SiIV from OIV], and by the frequent occurrence of absorptions affecting the blue side of the blend. Both factors may conspire to depress BLUE. The lower diagrams of Fig. 8 are again helpful to identify sources for which intensity ratios deviate significantly from the rest of the sample. SDSS

J102606.67+011459.0 shows a strong enhancement of CIV/HeII $\lambda$ 1640 and SiIV+OIV], confirming the trend seen in its BC.

#### 4.1.4. Correlation between diagnostic ratios

Fig. 9 shows a matrix of correlation coefficients for all diagnostic ratios which we considered in this work. The  $2\sigma$  confidence level of significance for the Spearman's rank correlation coefficient for 13 objects is achieved for  $\rho \approx 0.54$ . The highest degree of cor-

**Table 2.** Measurements in the 1900Å blend region.

SDSS JCODE	AlIII W	AlIII FWHM	AlIII Flux	CIII] FWHM	CIII] Flux	SiIII] Flux
(1)	(2)	(3)	(4)	(5)	(6)	(7)
J010657.94-085500.1	7.9	5560	5.41 ± 0.38	6050	2.88 ± 0.14	7.2 ± 0.93
J082936.30+080140.6	10.2	5710	7.43 ± 0.42	5950	2.39 ± 0.21	4.85 ± 0.66
J084525.84+072222.3	13.1	5510	6.04 ± 0.52	5570	4.25 ± 0.53	3.13 ± 0.08
J084719.12+094323.4	9.9	5410	9.24 ± 0.24	5630	4.63 ± 0.36	5.61 ± 0.73
J085856.00+015219.4	7.7	5520	4.57 ± 0.37	5660	3.98 ± 0.12	4.39 ± 0.58
J092641.41+013506.6	8.0	5550	4.82 ± 0.3	5720	6.53 ± 0.23	5.48 ± 0.96
J094637.83-012411.5	5.0	2730	3.54 ± 0.24	2090	6.38 ± 0.22	5.1 ± 0.67
J102421.32+024520.2	10.1	5520	6.15 ± 0.31	6080	3.31 ± 0.2	5.1 ± 0.39
J102606.67+011459.0	9.5	5590	7.7 ± 0.35	5470	1.83 ± 0.33	3.64 ± 0.3
J114557.84+080029.0	11.4	5520	8.74 ± 0.38	6060	5.91 ± 0.83	6.3 ± 0.81
J150959.16+074450.1	11.8	5530	6.44 ± 0.53	6090	7.62 ± 0.25	7.58 ± 1.32
J151929.45+072328.7	10.5	5320	7.37 ± 0.51	5310	5.6 ± 0.62	7.16 ± 1.12
J211651.48+044123.7	6.1	5550	4.21 ± 0.4	5620	5.29 ± 0.2	5.35 ± 0.7

NOTE—Columns are as follows: (1) SDSS name, (2) and (3) report the FWHM of AlIII and CIII] in km s<sup>-1</sup>; (4), (5) and (6) list the fluxes in units of 10<sup>-14</sup> erg s<sup>-1</sup>cm<sup>-2</sup> for AlIII, CIII], and SiIII].**Table 3.** Measurements in the CIV spectral region

SDSS JCODE	CIV W	CIV BC FWHM	CIV BC Flux	CIV BLUE Flux	HeII BC Flux	HeII BLUE Flux
(1)	(2)	(3)	(4)	(5)	(6)	(7)
J010657.94-085500.1	18.6	5530	6.35±1.04	13.46±0.13	1.79±0.46	1.93±0.65
J082936.30+080140.6	15.5	3710±670	1.83±0.4	11.86±0.03	0.8±0.11	1.72±0.69
J084525.84+072222.3	16.8	3760	5.04±0.68	11.11±0.21	1.06±0.15	1.87±0.81
J084719.12+094323.4	17.6	5520	11.53±0.53	13.24±0.07	2.14±0.61	2.1±1.19
J085856.00+015219.4	22.8	5460	9.84±0.82	11.39±0.09	0.65±0.32	1.28±0.48
J092641.41+013506.6	25.5	5550	7.79±1.98	7.08±0.08	1.94±0.33	1.47±0.39
J094637.83-012411.5	23.6	3670	15.63±0.6	5.89±0.09	1.87±0.39	1.76±0.7
J102421.32+024520.2	20.1	5640	6.74±0.45	10.9±0.08	1.9±0.19	2.19±1.07
J102606.67+011459.0	17.3	3700±650	6.92±1.22	12.23±0.05	0.82±0.34	1.15±0.32
J114557.84+080029.0	18.4	3500±700	6.84±0.3	12.57±0.03	2.01±0.5	2.26±1.02
J150959.16+074450.1	16.8	3530±690	4.19±0.84	9.73±0.22	2.21±0.14	1.48±0.74
J151929.45+072328.7	19.4	3470±590	5.47±0.41	12.04±0.16	1.52±0.09	2.14±0.24
J211651.48+044123.7	19.1	4750	13.04±0.68	3.01±0.24	0.99±0.03	1.77±0.69

NOTE. Columns are as follows: (1) SDSS name, (2) rest-frame equivalent width of the total CIV emission i.e., CIV BLUE+BC, in Å; (3) the FWHM of the CIV line in km s<sup>-1</sup>; Cols. (4) and (5) list fluxes of the CIV BC and BLUE line; Cols. (6) and (7) report fluxes of the BC and BLUE components for the HeIIλ1640 line. All fluxes are in units of 10<sup>-14</sup> erg s<sup>-1</sup>cm<sup>-2</sup>.

relation is found between the ratios CIV/HeIIλ1640 and CIV/SiIV(0.87), and between CIV/HeIIλ1640 and SiIV/HeIIλ1640 (0.81). A milder degree of correlation is found between AlIII/HeIIλ1640 and CIV/HeIIλ1640 (0.23) and SiIV/HeIIλ1640 (0.44). These results imply that SiIV and CIV are likely affected in a related way by a single parameter. The main parameter is expected to be  $T_e$ , and hence  $Z$  (Sect. 3.5.1). The AlIII (normalized to the HeIIλ1640 flux) line shows much lower values of the

correlation coefficient. While SiIV and CIV are basically the same line, the AlIII formation may not be exclusively collisional, as shown by the results of the CLOUDY simulations. Therefore there could be a different response to individual  $U$ ,  $n_H$  and optical depth variations. The prominence of CIII] with respect to SiIII] decreases with SiIV/HeIIλ1640 BLUE, CIV/HeIIλ1640, SiIV/HeIIλ1640 BLUE, and increases with CIV/SiIV+OIV]. Apparently the CIII]/SiIII] ratio is strongly affected by an increase

**Table 4.** Measurements in the  $\lambda 1400$  region.

SDSS JCODE	Siiv+Orv] BC FWHM	Siiv+Orv] BC Flux	Siiv+Orv] BLUE Flux
(1)	(2)	(3)	(4)
J010657.94-085500.1	5070	9.23 $\pm$ 1.4	6.24 $\pm$ 0.24
J082936.30+080140.6	5560	4.39 $\pm$ 0.81	7.3 $\pm$ 0.06
J084525.84+072222.3	5060	10.52 $\pm$ 0.58	2.69 $\pm$ 0.24
J084719.12+094323.4	5550	13.69 $\pm$ 0.86	3.79 $\pm$ 0.19
J085856.00+015219.4	6960	7.34 $\pm$ 0.69	8.55 $\pm$ 0.05
J092641.41+013506.6	5540	14.89 $\pm$ 0.45	4.05 $\pm$ 0.32
J094637.83-012411.5	4030	18.09 $\pm$ 0.7	3.29 $\pm$ 0.31
J102421.32+024520.2	5530	8.77 $\pm$ 0.64	4.06 $\pm$ 0.09
J102606.67+011459.0	5300	10.16 $\pm$ 0.57	4.01 $\pm$ 0.33
J114557.84+080029.0	3760	12.19 $\pm$ 1.22	5.71 $\pm$ 0.08
J150959.16+074450.1	3650	9.97 $\pm$ 0.75	5.86 $\pm$ 0.12
J151929.45+072328.7	3670	9.32 $\pm$ 1.05	4.48 $\pm$ 0.31
J211651.48+044123.7	4770	11.02 $\pm$ 0.77	0.81 $\pm$ 0.03

NOTE. Columns are as follows: (1) SDSS name, (2) the FWHM of the Siiv line in  $\text{km s}^{-1}$ . (3) and (4) list fluxes of the broad components and the blue component line in units of  $10^{-14} \text{ ergs}^{-1} \text{ cm}^{-2}$ .

**Table 5.** Intensity ratios for the BC and BLUE line components

SDSS JCODE	AlIII/Siiv] (BC)	CIII/Siiv] (BC)	Civ/Siiv (BC)	Civ/Hen $\lambda$ 1640 (BC)	Siiv/Hen $\lambda$ 1640 (BC)	Civ/AlIII (BC)	AlIII/Hen $\lambda$ 1640 (BC)	Civ/Hen $\lambda$ 1640 (BLUE)	Civ/Siiv+ Orv] (BLUE)	Siiv+ Orv]/ Hen $\lambda$ 1640 (BLUE)
(1)	(2)	(3)	(4)	(5)	(6)	(7)	(8)	(9)	(10)	(11)
J010657.94-085500.1	0.75 $\pm$ 0.11	0.4 $\pm$ 0.05	0.69 $\pm$ 0.15	3.55 $\pm$ 1.09	5.16 $\pm$ 1.55	1.17 $\pm$ 0.21	3.02 $\pm$ 0.81	6.98 $\pm$ 3	2.16 $\pm$ 0.58	3.24 $\pm$ 1.1
J082936.30+080140.6	1.53 $\pm$ 0.23	0.49 $\pm$ 0.08	0.42 $\pm$ 0.12	2.29 $\pm$ 0.6	5.48 $\pm$ 1.26	0.25 $\pm$ 0.06	9.28 $\pm$ 1.39	6.89 $\pm$ 3.75	1.62 $\pm$ 0.6	4.24 $\pm$ 1.69
J084525.84+072222.3	1.93 $\pm$ 0.17	1.36 $\pm$ 0.17	0.48 $\pm$ 0.07	4.76 $\pm$ 0.92	9.95 $\pm$ 1.48	0.83 $\pm$ 0.13	5.71 $\pm$ 0.93	5.93 $\pm$ 3.07	4.13 $\pm$ 1.23	1.43 $\pm$ 0.63
J084719.12+094323.4	1.65 $\pm$ 0.22	0.82 $\pm$ 0.12	0.84 $\pm$ 0.07	5.38 $\pm$ 1.55	6.39 $\pm$ 1.86	1.25 $\pm$ 0.07	4.31 $\pm$ 1.23	6.29 $\pm$ 4.74	3.5 $\pm$ 1.75	1.8 $\pm$ 1.02
J085856.00+015219.4	1.04 $\pm$ 0.16	0.91 $\pm$ 0.12	1.34 $\pm$ 0.17	15.25 $\pm$ 7.63	11.38 $\pm$ 5.71	2.15 $\pm$ 0.25	7.08 $\pm$ 3.54	8.87 $\pm$ 5.01	1.33 $\pm$ 0.57	6.66 $\pm$ 2.47
J092641.41+013506.6	0.88 $\pm$ 0.16	1.19 $\pm$ 0.21	0.52 $\pm$ 0.13	4.03 $\pm$ 1.23	7.69 $\pm$ 1.31	1.62 $\pm$ 0.42	2.49 $\pm$ 0.45	4.83 $\pm$ 1.92	1.75 $\pm$ 0.53	2.76 $\pm$ 0.77
J094637.83-012411.5	0.7 $\pm$ 0.1	1.25 $\pm$ 0.17	0.86 $\pm$ 0.05	8.34 $\pm$ 1.74	9.66 $\pm$ 2.02	4.41 $\pm$ 0.35	1.89 $\pm$ 0.41	3.35 $\pm$ 1.99	1.79 $\pm$ 0.8	1.87 $\pm$ 0.77
J102421.32+024520.2	1.2 $\pm$ 0.11	0.65 $\pm$ 0.06	0.77 $\pm$ 0.08	3.55 $\pm$ 0.43	4.61 $\pm$ 0.58	1.1 $\pm$ 0.09	3.23 $\pm$ 0.37	4.97 $\pm$ 3.09	2.68 $\pm$ 1.04	1.85 $\pm$ 0.9
J102606.67+011459.0	2.12 $\pm$ 0.2	0.5 $\pm$ 0.1	0.68 $\pm$ 0.13	8.48 $\pm$ 3.83	12.46 $\pm$ 5.23	0.9 $\pm$ 0.16	9.45 $\pm$ 3.96	10.6 $\pm$ 4.21	3.05 $\pm$ 0.9	3.47 $\pm$ 1.01
J114557.84+080029.0	1.39 $\pm$ 0.19	0.94 $\pm$ 0.18	0.56 $\pm$ 0.06	3.41 $\pm$ 0.87	6.07 $\pm$ 1.64	0.78 $\pm$ 0.05	4.36 $\pm$ 1.11	5.56 $\pm$ 3.76	2.2 $\pm$ 1.11	2.53 $\pm$ 1.14
J150959.16+074450.1	0.85 $\pm$ 0.16	1 $\pm$ 0.18	0.42 $\pm$ 0.09	1.9 $\pm$ 0.4	4.51 $\pm$ 0.44	0.65 $\pm$ 0.14	2.92 $\pm$ 0.3	6.58 $\pm$ 4.49	1.66 $\pm$ 0.77	3.96 $\pm$ 1.98
J151929.45+072328.7	1.03 $\pm$ 0.18	0.78 $\pm$ 0.15	0.59 $\pm$ 0.08	3.61 $\pm$ 0.35	6.14 $\pm$ 0.79	0.74 $\pm$ 0.08	4.86 $\pm$ 0.45	5.62 $\pm$ 1.66	2.69 $\pm$ 0.76	2.09 $\pm$ 0.28
J211651.48+044123.7	0.79 $\pm$ 0.13	0.99 $\pm$ 0.13	1.18 $\pm$ 0.1	13.12 $\pm$ 0.78	11.08 $\pm$ 0.84	3.1 $\pm$ 0.34	4.23 $\pm$ 0.42	1.7 $\pm$ 0.73	3.71 $\pm$ 0.67	0.46 $\pm$ 0.18
Median	1.04 $\pm$ 0.34	0.91 $\pm$ 0.17	0.68 $\pm$ 0.16	4.03 $\pm$ 2.395	6.39 $\pm$ 2.23	1.10 $\pm$ 0.42	4.31 $\pm$ 1.35	5.93 $\pm$ 0.96	2.2 $\pm$ 0.65	2.53 $\pm$ 0.81

in metallicity and more in general by ratios that are indicative of “extremeness” in our sample. For BLUE, the two main independent  $Z$  estimators are correlated ( $\rho \approx 0.68$ ).

#### 4.2. Analysis of $Z$ distributions: global inferences on sample

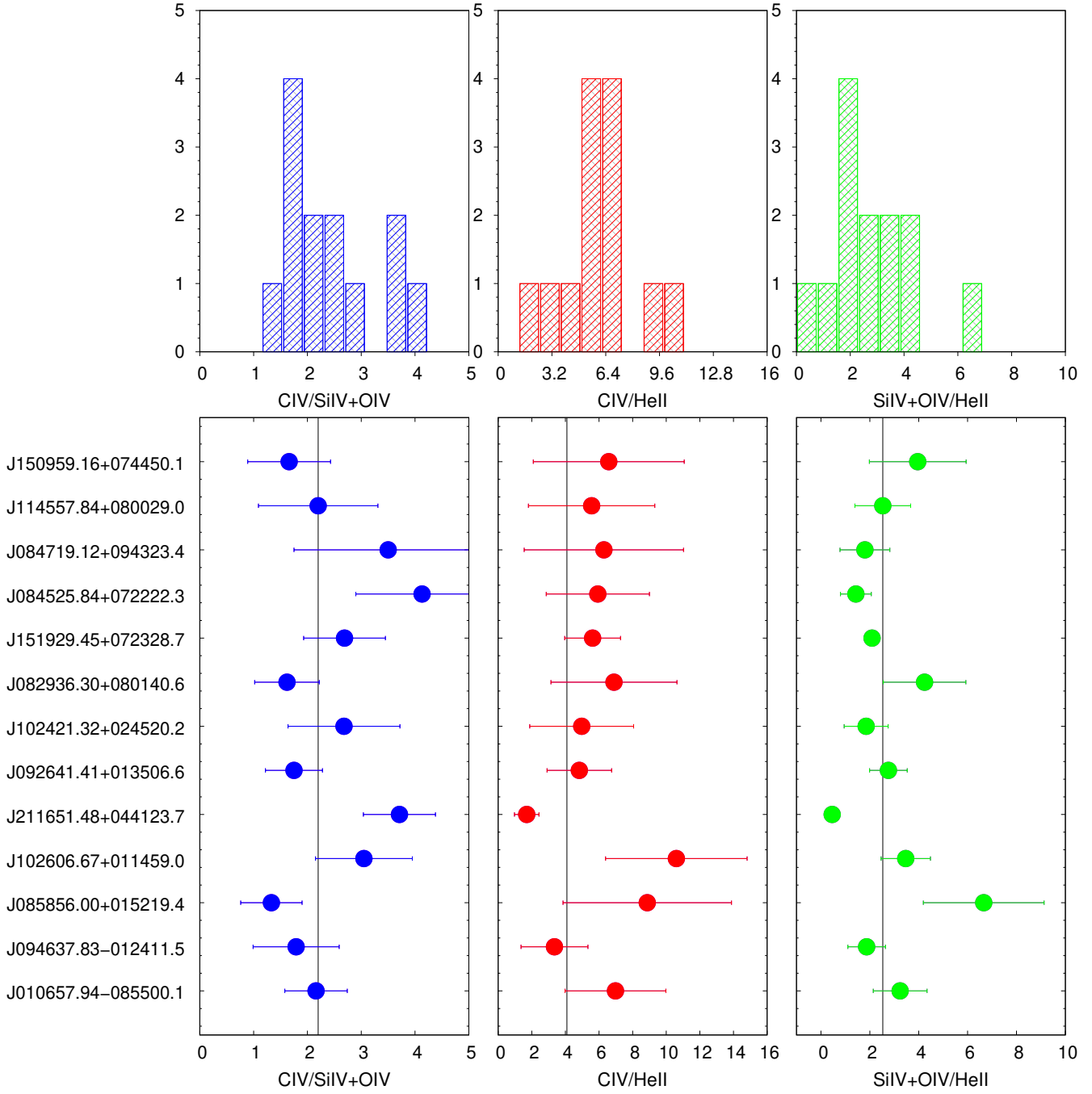
##### 4.2.1. Fixed ( $U, n_H$ )

We propagated the diagnostic intensity ratios measured on the BC and BLUE components with their lower and upper uncertainties following the relation between ratios and  $Z$  in the Figures 2, for the fixed physical conditions assumed in the low- and high-ionization region. The results are reported in Table 6 and Table 7 for the BC and for the blueshifted component, respec-

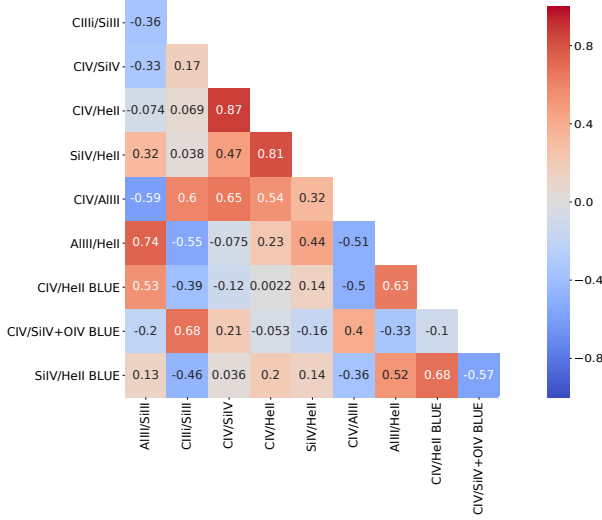
tively. The last row reports the median values of the individual sources  $Z$  estimates with the sample SIQR. The distributions are shown in Figs. 10 and 11, along with a graphical presentation of each source and its associated uncertainties.

Table 6 and Table 7 permit to quantify the systematic differences that are apparent in Figs. 10 and 11. The agreement between the various estimators is in good on average (the medians scatter around  $\log Z \approx 1$  by less than 0.2 dex). However, there are systematic differences between the  $Z$  obtained from the various diagnostic ratios. Siiv and AlIII over Hen $\lambda$ 1640 apparently overestimate the  $Z$  by a factor 2 with respect to Civ/Hen $\lambda$ 1640. The out-of-scale values of Civ/Siiv and Civ/AlIII may suggest that metallicity scaling according to solar pro-





**Figure 8.** Distribution of diagnostic intensity ratios based on the BLUE components (top) for  $\text{CIV}/\text{SiIV}+\text{OIV}$  (blue),  $\text{CIV}/\text{HeII}\lambda 1640$  (red) and  $\text{SiIV}+\text{OIV}/\text{HeII}\lambda 1640$  (green). The lower panels show results and associated uncertainties for individual sources with the same color-coding as histograms, as in the previous Figure. Vertical black line represents median value of ratios measurements.



**Figure 9.** The correlation matrix between diagnostic ratios in BC and BLUE. The numbers in each square show the Spearman rank correlation coefficient. Red colors indicate a positive correlation, blue colors indicate a negative correlation..

portion may not be strictly correct (Sect. 5.6). In the case of BLUE, several estimates from CIV/HeII $\lambda$ 1640 strongly deviate from the ones obtained with the other ratios, due to the non-monotonic behavior of the relation between  $Z$  and CIV/HeII $\lambda$ 1640, right in the range of metallicity that is expected.

The median values of all three ratios consistently suggest high metallicity with a firm lower limit  $Z \approx 10$ , and in the range  $10Z_{\odot} \lesssim Z \lesssim 100Z_{\odot}$ . There is apparently a systematic difference between BC and BLUE, in the sense that  $Z$  derived from the BC is systematically higher than  $Z$  from blue. The difference is small in the case of CIV/HeII $\lambda$ 1640 but is significant in the case of SiIV+OIV]/HeII $\lambda$ 1640, where  $Z$  from BLUE are a factor of 10 lower. We have stressed earlier that there are often absorptions affecting the BLUE of SiIV+OIV]/HeII $\lambda$ 1640. Absorptions and the blending with CII $\lambda$ 1332 and SiIV BC lines make it difficult to properly define the continuum underlying the  $\lambda$ 1400 blend at negative radial velocities. We think that the SiIV+OIV] BLUE intensity estimate is more of a lower limit. Another explanation might be related to the assumption of a constant density and  $U$  for all sources. While there are observational constraints supporting this condition for the BC (Panda et al. 2018, 2019, 2020b), there are no strong clues to the BLUE properties, save a high ionization degree.

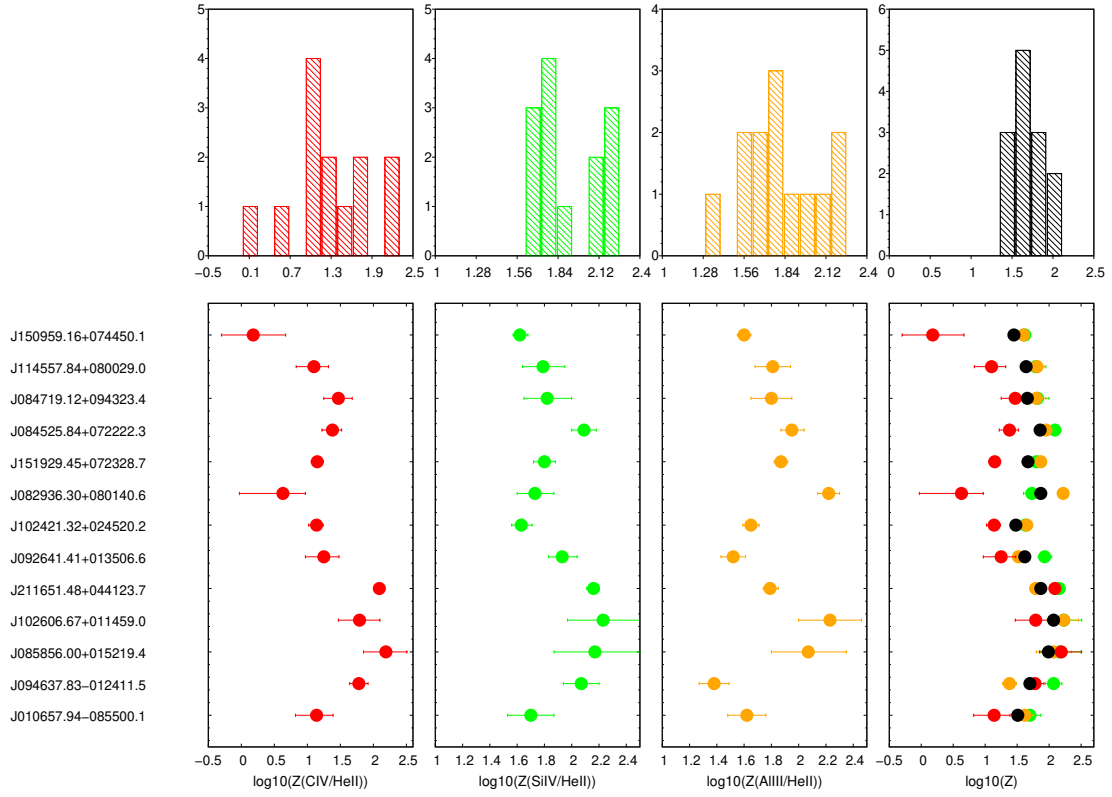
#### 4.3. $Z$ for individual sources for fixed $U$ , $n_H$

Table 8 reports the  $Z$  estimates for the BC, BLUE, and a combination of BC and BLUE for each individual object. The values reported are the median values of the individual objects' estimates from the different ratios. For BC, the three ratios of Table 6 were always used. The last column of Table 8 reports the number of ratios used from the BLUE component. Here the  $Z$  value for each object is computed by vetting the ratios according to concordance. If the discordance is not due on physical ground, but rather to instrumental problems (for example, contamination by absorption lines, non linear dependence on  $Z$  of some ratios), a proper strategy is to use estimators such as the median that eliminate discordant values even for small sample sizes ( $n \geq 3$ ). Measuring medians and SIQR is an efficient way to deal with the measurements of large samples of objects. All estimates  $\log Z \lesssim 0$  were excluded, as either the product of heavy absorptions (SiIV+OIV]/HeII $\lambda$ 1640) or of difficulties in relating the ratio (CIV/HeII $\lambda$ 1640) to  $Z$ ; apart from J211651.48+044123.7, the upper uncertainty of the negative estimates is so large that  $Z$  is actually unconstrained. The difference between BLUE and BC is even more evident: the median (last row) indicates a factor  $\approx 6$  difference between BLUE and BC. The BC suggests a median  $Z \approx 60Z_{\odot}$ , while the BLUE  $Z \approx 10Z_{\odot}$ . The assumption that the wind and disk component have the same  $Z$  in each object is a reasonable one, with the caveats mentioned in Sect. 5.6. Therefore the two estimates, for BLUE and BC could be considered two independent estimators of  $Z$ . If the two estimates are combined for each individual object,  $10Z_{\odot} \lesssim Z \lesssim 100Z_{\odot}$ , with a median value of  $Z \approx 20Z_{\odot}$ .

#### 4.4. Estimates of $Z$ relaxing the constraints on $U$ and $n_H$

The  $Z$  estimates for the BC are mainly based on the three ratios involving HeII $\lambda$ 1640 normalization. To gain a global, bird's eye view of the  $Z$  dependence on the physical parameters, we assigned a score from 0 to 3 and considered the domain of the parameter space  $U$ ,  $n_H$ ,  $Z$  for which there is agreement with all the three diagnostic ratios. The left panels of Fig. 12 and of Fig. 13 shows the 3D space  $U$ ,  $n_H$ ,  $Z$  where each point in space correspond to an element of the grid of CLOUDY the parameter space compatible with *all three* observed ratios within the uncertainties. The case shown in Fig. 12 and in Fig. 13 is the one with the median values of the sample objects.

Similar considerations can be made if we consider the  $\chi^2$  behavior. We compute the  $\chi^2$  in the following form, to identify the value of the metallicity for median values of the diagnostic ratios and for the diagnostic ratios of



**Figure 10.** (Upper panel) Distribution of metallicity measurements for broad component obtained from ratios C IV/He II  $\lambda$ 1640 (red), Si IV/He II  $\lambda$ 1640 (green), Al III/He II  $\lambda$ 1640 (orange) and the mean metallicity obtained from all ratios (black). (Lower panel) Results and associated uncertainties for individual sources with the same color-coding as histograms. The last panel contains all metallicity measurements and the mean of them for each object.

**Table 6.** Metallicity ( $\log Z$ ) of the BC assuming fixed  $U$ ,  $n_H$

SDSS JCODE	C IV/He II $\lambda$ 1640	Si IV/He II $\lambda$ 1640	Al III/He II $\lambda$ 1640
J010657.94-085500.1	$1.14^{+0.25}_{-0.32}$	$1.7^{+0.34}_{-0.17}$	$1.62^{+0.14}_{-0.14}$
J085856.00+015219.4	$2.19^{+0.32}_{-0.34}$	$2.17^{+0.63}_{-0.3}$	$2.07^{+0.28}_{-0.27}$
J082936.30+080140.6	$0.63^{+0.34}_{-0.66}$	$1.73^{+0.27}_{-0.13}$	$2.22^{+0.08}_{-0.08}$
J084525.84+072222.3	$1.38^{+0.14}_{-0.16}$	$2.09^{+0.18}_{-0.09}$	$1.95^{+0.09}_{-0.08}$
J084719.12+094323.4	$1.47^{+0.21}_{-0.22}$	$1.82^{+0.35}_{-0.17}$	$1.8^{+0.15}_{-0.15}$
J092641.41+013506.6	$1.25^{+0.23}_{-0.28}$	$1.93^{+0.21}_{-0.1}$	$1.52^{+0.09}_{-0.09}$
J094637.83-012411.5	$1.78^{+0.14}_{-0.14}$	$2.07^{+0.26}_{-0.13}$	$1.38^{+0.11}_{-0.11}$
J102421.32+024520.2	$1.14^{+0.1}_{-0.12}$	$1.63^{+0.15}_{-0.07}$	$1.65^{+0.06}_{-0.06}$
J102606.67+011459.0	$1.79^{+0.31}_{-0.32}$	$2.23^{+0.54}_{-0.26}$	$2.23^{+0.23}_{-0.23}$
J114557.84+080029.0	$1.10^{+0.22}_{-0.27}$	$1.79^{+0.31}_{-0.15}$	$1.81^{+0.13}_{-0.13}$
J150959.16+074450.1	$0.18^{+0.49}_{-0.48}$	$1.62^{+0.11}_{-0.05}$	$1.6^{+0.05}_{-0.05}$
J151929.45+072328.7	$1.15^{+0.09}_{-0.09}$	$1.8^{+0.16}_{-0.08}$	$1.87^{+0.05}_{-0.05}$
J211651.48+044123.7	$2.09^{+0.04}_{-0.04}$	$2.16^{+0.09}_{-0.05}$	$1.79^{+0.06}_{-0.05}$
Median	$1.37 \pm 0.32$	$1.82 \pm 0.18$	$1.80 \pm 0.165$

NOTE—Columns: (1) SDSS identification, (2), (3) and (4) metallicity values for C IV/He II  $\lambda$ 1640 Si IV+O IV]/He II  $\lambda$ 1640 and Al III/He II  $\lambda$ 1640 with uncertainties.

**Table 7.** Metallicity ( $\log Z$ ) of BLUE assuming fixed  $U$ ,  $n_H$

SDSS JCODE	Si IV+O IV]/He II $\lambda$ 1640	C IV/Si IV+O IV]	C IV/He II $\lambda$ 1640
J010657.94-085500.1	$1.01^{+0.13}_{-0.15}$	$0.89^{+0.14}_{-0.13}$	$1.37^{+0.32}_{-2.02}$
J082936.30+080140.6	$1.11^{+0.15}_{-0.16}$	$1.04^{+0.17}_{-0.19}$	$1.36^{+0.39}_{-2.18}$
J084525.84+072222.3	$0.63^{+0.21}_{-0.2}$	$0.63^{+0.1}_{-0.08}$	$1.16^{+0.48}_{-2.12}$
J084719.12+094323.4	$0.73^{+0.27}_{-0.25}$	$0.68^{+0.22}_{-0.14}$	$1.25^{+0.57}_{-2.36}$
J085856.00+015219.4	$1.29^{+0.22}_{-0.15}$	$1.17^{+0.23}_{-0.25}$	$1.57^{+0.34}_{-2.06}$
J092641.41+013506.6	$0.94^{+0.12}_{-0.13}$	$1.00^{+0.14}_{-0.16}$	$-0.56^{+1.96}_{-1.05}$
J094637.83-012411.5	$0.75^{+0.2}_{-0.18}$	$0.99^{+0.2}_{-0.22}$	$-1.01^{+2.21}_{-1.63}$
J102421.32+024520.2	$0.75^{+0.23}_{-0.22}$	$0.79^{+0.19}_{-0.14}$	$-0.51^{+2.11}_{-0.68}$
J102606.67+011459.0	$1.04^{+0.11}_{-0.13}$	$0.73^{+0.13}_{-0.09}$	$1.68^{+0.23}_{-0.29}$
J114557.84+080029.0	$0.9^{+0.19}_{-0.22}$	$0.88^{+0.25}_{-0.21}$	$1.02^{+0.68}_{-2.17}$
J150959.16+074450.1	$1.09^{+0.19}_{-0.22}$	$1.02^{+0.22}_{-0.23}$	$1.31^{+0.5}_{-2.32}$
J151929.45+072328.7	$0.81^{+0.06}_{-0.07}$	$0.78^{+0.14}_{-0.1}$	$1.05^{+0.39}_{-0.61}$
J211651.48+044123.7	$-0.34^{+0.58}_{-0.52}$	$0.67^{+0.06}_{-0.06}$	$-1.47^{+0.27}_{-0.24}$
Medians	$1.160 \pm 0.935$	$0.90 \pm 0.16$	$0.88 \pm 0.16$

NOTE—Columns: (1) SDSS identification, (2), (3) and (4) metallicity values for Si IV+O IV]/He II  $\lambda$ 1640 C IV/Si IV+O IV] and C IV/He II  $\lambda$ 1640 with uncertainties.

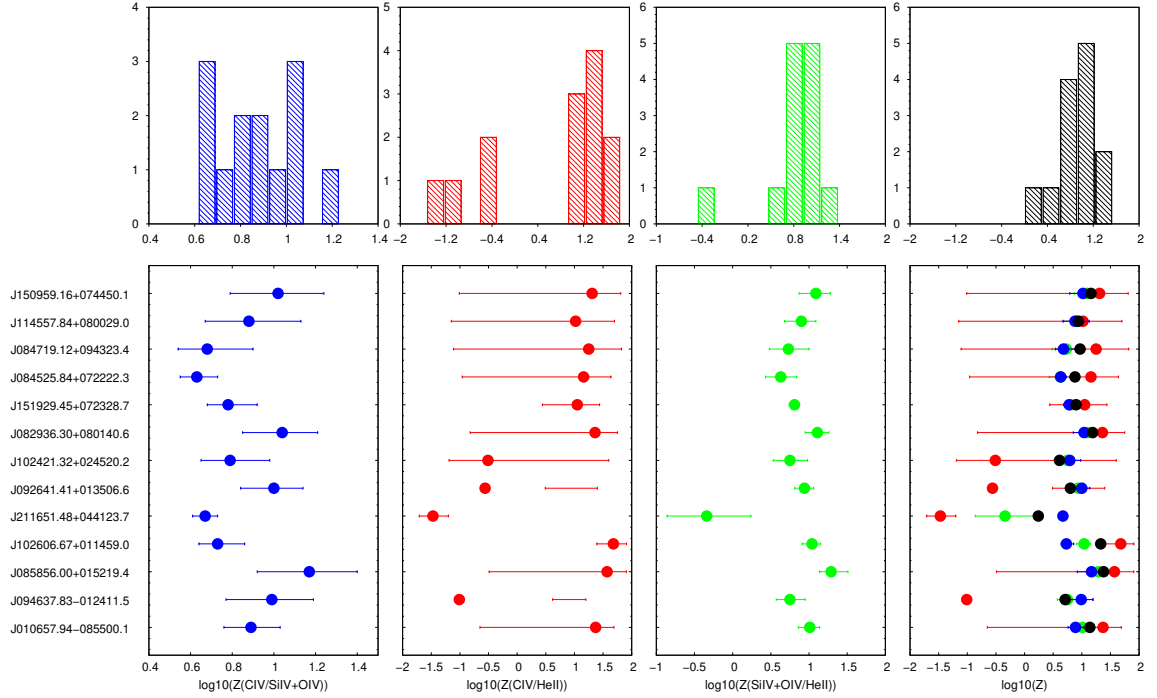


**Figure 11.** (Upper panel) Distribution of metallicity measurements for blue component obtained from ratios: C IV/Si IV+O IV] (blue), C IV/He II λ1640 (red), Si IV+O IV]/He II λ1640 (green) and the mean metallicity obtained from all ratios (black). (Lower panel) Results and associated uncertainties for individual sources with the same color-coding as histograms. The last panel contains all metallicity measurements and the mean of them for each object.

**Table 8.** Metallicity ( $\log Z$ ) of individual quasars assuming fixed  $U$ ,  $n_H$

SDSS JCODE	BC	BLUE	Combined	#
J010657.94-085500.1	$1.620 \pm 0.28$	$1.01 \pm 0.24$	$1.370 \pm 0.355$	3
J094637.83-012411.5	$1.780 \pm 0.35$	$0.99 \pm 0.12$	$1.38 \pm 0.400$	2
J085856.00+015219.4	$2.17 \pm 0.06$	$1.29 \pm 0.20$	$1.570 \pm 0.215$	3
J102606.67+011459.0	$2.23 \pm 0.22$	$1.04 \pm 0.475$	$1.600 \pm 0.445$	3
J211651.48+044123.7	$2.09 \pm 0.185$	$0.67 \pm \dots$	$2.09 \pm 0.185$	1
J092641.41+013506.6	$1.52 \pm 0.34$	$1.00 \pm 0.03$	$1.25 \pm 0.26$	2
J102421.32+024520.2	$1.629 \pm 0.255$	$0.79 \pm 0.02$	$1.14 \pm 0.42$	2
J082936.30+080140.6	$1.730 \pm 0.795$	$1.11 \pm 0.16$	$1.359 \pm 0.280$	2
J151929.45+072328.7	$1.799 \pm 0.36$	$0.81 \pm 0.135$	$1.049 \pm 0.410$	3
J084525.84+072222.3	$1.950 \pm 0.355$	$0.63 \pm 0.265$	$1.159 \pm 0.485$	3
J084719.12+094323.4	$1.799 \pm 0.175$	$0.73 \pm 0.285$	$1.25 \pm 0.460$	3
J114557.84+080029.0	$1.790 \pm 0.355$	$0.90 \pm 0.07$	$1.019 \pm 0.360$	3
J150959.16+074450.1	$1.600 \pm 0.72$	$1.09 \pm 0.145$	$1.309 \pm 0.290$	3
Median	$1.79 \pm 0.16$	$1.00 \pm 0.13$	$1.31 \pm 0.11$	3

NOTE—Columns: (1) SDSS identification, (2), (3) and (4) metallicity medians for BC, BLUE and the combination of the two, with uncertainties. Column (5) yields the number of ratios used for the BLUE estimates. No uncertainty is reported for BLUE of SDSS J211651.48+044123.7 since only one ratio was used.

individual objects relaxing the assumption of fixed den-

sity and ionization parameters. For each object  $k$ , and for each component  $c$ , we can write:

$$\chi^2_{kc}(n_H, U, Z) = \sum_i w_{ci} \left( \frac{R_{kci} - R_{kci, \text{mod}}(n_H, U, Z)}{\delta R_{kci}} \right)^2 \quad (8)$$

where the summation is done over the available diagnostic ratios, and the  $\chi^2$  is computed with respect to the results of the CLOUDY simulations as a function of  $U$ ,  $n_H$ , and  $Z$  (subscript ‘mod’). Weights  $w_{ci} = 1$  were assigned to C IV/He II λ1640, Si IV/He II λ1640, and Al III/He II λ1640;  $w_{ci} = 0$  or  $0.5$  were assigned to C IV/Al III and C IV/Si IV. For BLUE, the three diagnostic ratios were all assigned  $w_{ci} = 1$ .

The distribution of the data point for the median  $\pm$  SIQR values in Fig. 12 is constrained in a relatively narrow range of  $U$ ,  $n_H$ ,  $Z$ , at very high density, low ionization, and high metallicity. Within the limit in  $U$ ,  $n_H$ , the distribution of  $Z$  is flat and thin, around  $Z \sim 100Z_\odot$ . This implies that, for a change of the  $U$  and  $n_H$  within the limits allowed by the data, the estimate of  $Z$  is stable and independent on  $U$  and  $n_H$ . Table 8 reports the individual  $Z$  estimates and the SIQR for the sources in the sample (the last row is the median).



By far less constrained is the situation for BLUE. Fig. 13 shows the parameter spaces for the 3 ratios and  $\chi^2$  distributions. The spread in ionization and density is very large, although the concentration of data points is higher in the case of low  $n_{\text{H}}$  ( $\log n_{\text{H}} \sim 8-9$  [ $\text{cm}^{-3}$ ]) and high ionization ( $\log U \sim 0$ ). At any rate the spread of the data points indicate that solution at low ionization and high density are possible. The results for individual sources tend to disfavor this scenario for the wide majority of the objects, but the properties of the gas emitting the BLUE are less constrained than for the BC. What is missing for BLUE is especially a firm diagnostic of density that in the case of BC is provided mainly by the ratio  $\text{AlIII}/\text{HeII}\lambda 1640$ . Results on  $Z$  are however as stable as for the BC, even if the dispersion is large, and suggest values in the range  $10 \lesssim Z \lesssim 100Z_{\odot}$ .

Summing up, all meaningful estimators converge toward high  $Z$  values,  $Z \gtrsim 10Z_{\odot}$ . Ratios  $\text{CIV}/\text{SiIV}$  significantly less than  $< 1$  are not predicted in the parameter space.  $\text{SiIV}/\text{HeII}\lambda 1640$  seems to give the largest estimates of  $Z$ . Also the high  $\text{AlIII}/\text{CIV}$  requires extremely high values of  $Z$ . A conclusion has to be tentative, considering the possible systematic errors affecting the estimates of the CIV and SiIV intensities: for CIV, the BC in the most extreme cases is often buried under an overwhelming BLUE; a fit is not providing a reliable estimate of the BC (by far the fainter component) but provides a reliable BLUE intensity; for SiIV we may overestimate the intensity due to “cancellation” of the BLUE by absorptions. This said, the present data are consistent with the possibility of a selective enhancement of Al and Si, as already considered by Negrete et al. (2012). The issue will be briefly discussed in Sect. 5.

At any rate, the absence of correlation between BLUE and BC parameters (Fig. 9), the difference in the diagnostic ratios and differences in inferred  $Z$ , as well as the results for individual sources described below justify the approach followed in the paper to maintain a separation between BLUE and BC. The meaning of possible systematic differences between the BC and BLUE are further discussed in §5.

#### 4.4.1. Individual sources

The best  $n_{\text{H}}$ ,  $U$ , and  $Z$  for each object have been obtained by minimizing the  $\chi^2$  as defined in Eq. 8, and they are reported in Table 9. The last two rows list the minimum  $\chi^2$  values for the median (with the SIQR of the sample) and for the median on the medians reported for individual sources. In other words, the choice of the best physical conditions was obtained by minimizing the sum of the deviations between the model predictions and the observer diagnostic ratios. The obtained value

of  $Z$  cover the range  $20 \lesssim Z \lesssim 500$ , with 10 out of 13 sources with  $50 \lesssim Z \lesssim 200Z_{\odot}$ , and medians of intensity ratios yielding  $Z \sim 100Z_{\odot}$ . There is some spread in the ionization parameter values,  $-3.75 \lesssim U \lesssim -1.75$ , but in all cases indicating low or very low ionization level. The hydrogen density is very high, in only one case  $\log n_{\text{H}} \approx 11.75$ , and in several cases  $n_{\text{H}}$  reaches  $10^{14} \text{ cm}^{-3}$ . The median values are  $Z = 100Z_{\odot}$ ,  $\log U = -2.5$ ,  $\log n_{\text{H}} = 13$ , therefore validating the original assumption of  $\log U = -2.5$ ,  $\log n_{\text{H}} = 12$  for fixed physical condition. The result for individual sources confirm the scenario of Fig. 12 for the wide majority of the sample sources. The higher  $n_{\text{H}}$  values are consistent with recent inferences for the low-ionization BLR derived from Temple et al. (2020), based on the FeIII UV emission which is especially prominent in the UV spectra of xA quasars (Martínez-Aldama et al. 2018). It is interesting to note that borderline objects ( $\text{AlIII}/\text{SiIII} \approx 0.5$ ,  $\text{CIII}/\text{SiIII} \approx 1$ ) show higher values of the ionization parameter ( $\log U \approx -1.75$ ), and also the lowest value of  $Z$  for the BC ( $\approx 20Z_{\odot}$ ).

The inferences are less clear from BLUE (Table 10). In some cases, the permitted volume in the 3D parameter space for individual sources covers a broad range in  $U$  and  $n_{\text{H}}$  as for the median. In some others the volume is more limited but the  $n_{\text{H}}$  can be very high  $\log n_{\text{H}} \sim 14$ . Most sources show high degree of ionization,  $-1 \lesssim \log U \lesssim 0$ , and only in one case SDSS J102606.67+011459.0 there is apparently a low-ionization solution with  $U$  comparable to that of the low-ionization BLR. The median suggests  $\log n_{\text{H}} \sim 8.25$ ,  $\log U \sim -0.5$ , close to the values that we assumed for the fixed ( $U$ ,  $n_{\text{H}}$ ) approach. The results on metallicity suggest in most cases  $Z \gtrsim 20Z_{\odot}$ , even if  $Z$  for the median is  $Z = 10Z_{\odot}$ . However, within  $3\sigma$  from the minimum  $\chi^2$ ,  $Z$  values up to 100 are also possible.

In summary, the low-ionization BLR of xA sources seems to be consistently characterized by extremely low ionization, high density and very high metallicity, under the assumption that  $Z$  scales with the solar chemical composition. Diagnostics on BLUE is less constraining, and measurements are more difficult. The 0-order results are however consistent again with high metallicity  $Z \gtrsim 10Z_{\odot}$ . Inferences on  $Z$  are in agreement with the case for fixed physical conditions, as the  $Z$  determinations are weakly dependent on  $U$ ,  $n_{\text{H}}$ .

## 5. DISCUSSION

### 5.1. A method to estimate $Z$

The determination of the metal content of the broad line emitting region of xA quasars was made possible by the following procedure:

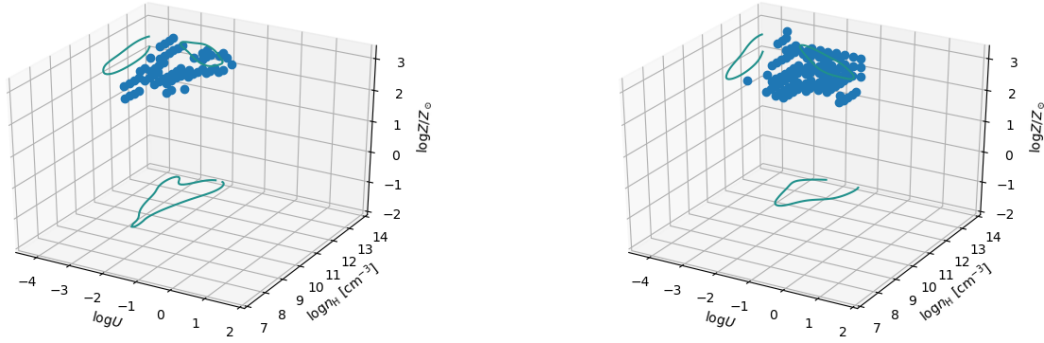


**Figure 12.** The parameter space  $n_H$ ,  $U$ ,  $Z$ . Left: data points in 3D space are elements in the grid of the parameter space that are in agreement with the three main diagnostic ratios used for the BC, within the SIQR of the median estimate from Table 5. The individual contour was smoothed with a Gaussian kernel. Right: data points in the parameter space selected for not being different from  $\chi^2_{\min}$  within a confidence level of  $3\sigma$ .

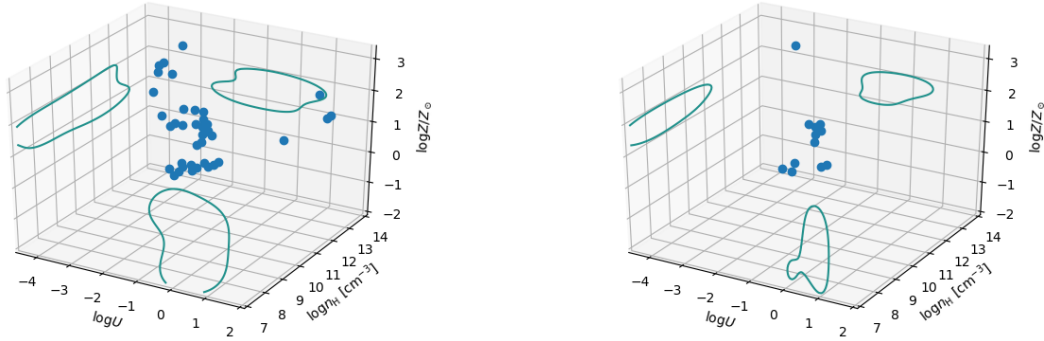


**Figure 13.** The parameter space  $n_H$ ,  $U$ ,  $Z$ . Left: data points in 3D space are elements in the grid of the parameter space that are in agreement with the three main diagnostic ratios used for BLUE, within the SIQR of the median estimate from Table 5. The individual contour was smoothed with a Gaussian kernel. Right: data points in the parameter space selected for not being different from  $\chi^2_{\min}$  within a confidence level of  $3\sigma$ .

1. the estimation of an accurate redshift. Even if all lines are affected by significant blueshifts which reduce the values of measured redshift, in the absence of information from the  $H\beta$  spectral range the  $AlIII$  and the  $\lambda 1900$  blend can be used as proxies of proper redshift estimators. The blueshifts are the smallest in the intermediate ionization lines at  $\lambda 1900$  (del Olmo et al., in preparation).
2. the separation of the BC and BLUE, for  $CIV$  and the  $\lambda 1400$  blend. The line width of the individual components of the  $AlIII$  doublet can be used as a template BC. The component BLUE is defined as the excess emission on the blue side of the BC.
3. a first estimate of metallicity can be obtained from the assumption that the low-ionization BLR associated with the BC and wind/outflow component associated with BLUE can be described by similar physical conditions in different objects. Several diagnostic ratios can be associated with the intensity ratios predicted by an array of photoionization simulations, namely
  - for the BC:  $AlIII/HeII\lambda 1640$ ,  $CIV/HeII\lambda 1640$ ,  $SiIV/HeII\lambda 1640$ , assuming  $(\log U, \log n_H) = (-2.5, 12)$  or  $(\log U, \log n_H) = (-2.5, 13)$
  - for the BLUE:  $CIV/HeII\lambda 1640$ ,  $SiIV+OIV/HeII\lambda 1640$ ,  $CIV/SiIV+OIV]$  assuming  $(\log U, \log n_H) = (0, 9)$ .

**Table 9.**  $Z$ ,  $U$ ,  $n_{\text{H}}$  of individual sources and median derived from the BC

SDSS JCODE	$Z [Z_{\odot}]$	$\log U$	$\log n_{\text{H}}$
(1)	(2)	(3)	(4)
J010657.94-085500.1	200	-2.25	14
J094637.83-012411.5	20	-1.25	13
J085856.00+015219.4	100	-2.25	12
J102606.67+011459.0	500	-2.00	13.75
J211651.48+044123.7	50	-1.75	11.75
J092641.41+013506.6	50	-1.75	13.75
J102421.32+024520.2	100	-2.50	13.5
J082936.30+080140.6	200	-3.75	13.75
J151929.45+072328.7	500	-3.75	14
J084525.84+072222.3	200	-2.50	13.75
J084719.12+094323.4	100	-2.5	13
J114557.84+080029.0	100	-2.00	14
J150959.16+074450.1	100	-2.25	14
Median	100	-2.5	13
$\mu_{\frac{1}{2}}$ (Medians)	100 $\pm$ 50	-2.25 $\pm$ 0.25	13.75 $\pm$ 0.5

NOTE—Columns: (1) SDSS identification, (2), (3) and (4)  $Z$  in units of  $Z_{\odot}$ ,  $\log U$  and  $\log n_{\text{H}}$  in  $\text{cm}^{-3}$  in the same order.**Table 10.**  $Z$ ,  $U$ ,  $n_{\text{H}}$  of individual sources and median derived from BLUE

SDSS JCODE	$Z [Z_{\odot}]$	$\log U$	$\log n_{\text{H}}$
(1)	(2)	(3)	(4)
J010657.94-085500.1	50	-0.75	10
J082936.30+080140.6	50	0.75	8
J084525.84+072222.3	50	-1	7.25
J084719.12+094323.4	50	-0.25	8
J085856.00+015219.4	20	-0.25	14
J102606.67+011459.0	200	-2.5	8.75
J114557.84+080029.0	10	-0.25	8
J150959.16+074450.1	10	-1	11
J151929.45+072328.7	50	-2	11.25
Median	10	-0.5	8.25
$\mu_{\frac{1}{2}}$ (Medians)	50 $\pm$ 15	-0.75 $\pm$ 0.375	8.75 $\pm$ 1.5

NOTE—Columns: (1) SDSS identification, (2), (3) and (4)  $Z$  in units of  $Z_{\odot}$ ,  $\log U$  and  $\log n_{\text{H}}$  in  $\text{cm}^{-3}$  in the same order.

- Estimates can be refined for individual sources relaxing the constant ( $\log U$ ,  $\log n_{\text{H}}$ ) assumptions. Tight constraints can be obtained for the BC. The BLUE is more problematic, because of both observational difficulties and the absence of unambiguous diagnostics.

Our method relies on ratios involving  $\text{HeII}\lambda 1640$  that have not been much considered in previous literature. In addition, we have considered fixed SED, turbulence

(equal to 0), and column density in the simulations ( $N_{\text{c}} = 10^{23}$ ) as fixed. The role of turbulence is further discussed in Sect. 5.5, and is found to be not relevant unlike in the case of  $\text{FeII}$  emission in the optical spectral range, where effects of self- and  $\text{Ly}\alpha$ -fluorescence are important, (e.g., Verner et al. 1999; Panda et al. 2018), while the  $N_{\text{c}}$  effect is most likely negligible.

Extension of the method to the full Population A is a likely possibility, since we do not expect a very strong effect of the SED on the metallicity estimate, as long as the SED has a prominent big blue bump, as it seems to be case for Population A. The role of SED is likely important if the method has to be extended to sources of Pop. B along the main sequence. Intensity ratios involving  $\text{HeII}\lambda 1640$  are difficult to measure in the xA spectra, but may be more accessible for Population B spectra. Ferland et al. (2020) have shown significant differences in the SED as a function of  $L/L_{\text{Edd}}$ , with a much flatter SED at low  $L/L_{\text{Edd}}$ . The extension to Pop. B would therefore require a new dedicated array of simulations.

## 5.2. Accretion parameters of sample sources

The bolometric luminosity has been computed assuming a flat  $\Lambda$ CDM cosmological model with  $\Omega_{\Lambda} = 0.7$ ,  $\Omega_m = 0.3$ , and  $H_0 = 70 \text{ km s}^{-1} \text{ Mpc}^{-1}$ . Following Marziani & Sulentic (2014) we decided to use  $\text{AlIII}$  as virial broadening estimator for computing the  $M_{\text{BH}}$ . Our estimates adopt two different scaling laws: (1) the scaling laws of Vestergaard & Peterson (2006) for CIV and a second, unpublished one based on  $\text{AlIII}$  (del Olmo et al., in preparation). Eddington ratios have been obtained using the Eddington luminosity  $L_{\text{Edd}} \approx 1.3 \times 10^{38} (M_{\text{BH}}/M_{\odot}) \text{ erg s}^{-1}$ . The luminosity range of the sample is very limited, less than a factor 3,  $46.8 \lesssim \log L \lesssim 47.3$ , in line with the requirement of similar redshift and high flux values. Correspondingly, the  $M_{\text{BH}}$  and the Eddington ratio are constrained in the range  $8.8 \lesssim \log M_{\text{BH}} \lesssim 9.5$  and  $-0.55 \lesssim \log L/L_{\text{Edd}} \lesssim 0.18$ , respectively. The  $M_{\text{BH}}$  sample dispersion is relatively small, with  $\log M_{\text{BH}} \sim 9.4 \pm 0.2 [M_{\odot}]$ . The scatter in  $M_{\text{BH}}$  and  $L/L_{\text{Edd}}$  is reduced to  $\approx 0.1$  dex if we exclude one object with the lowest  $M_{\text{BH}}$  and highest  $L/L_{\text{Edd}}$ . Applying a small correction (10%) to the FWHM to account for an excess broadening in  $\text{AlIII}$  due to non-virial motions will decrease the  $M_{\text{BH}}$  by 0.1 dex (as found by Negrete et al. 2018 for  $\text{H}\beta$ ), and increase  $L/L_{\text{Edd}}$  correspondingly. If this correction is applied the median  $L/L_{\text{Edd}}$  is  $\approx 0.6$ . Using the CIV BC FWHM as a virial broadening estimator, also decreasing  $M_{\text{BH}}$  median estimate by 0.1 dex, The accretion parameters are consistent with extreme quasars of Population A at high mass and luminosity; they are mainly at the

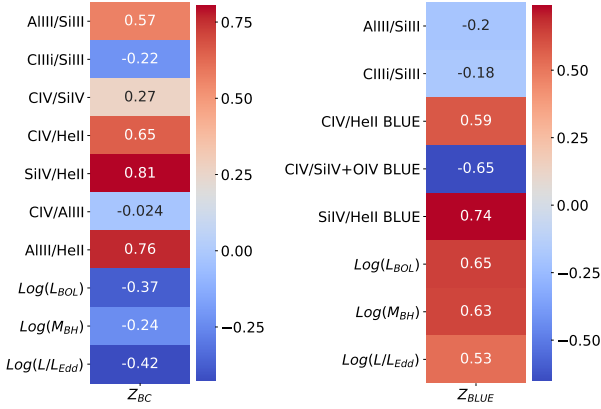


**Figure 14.** Left panel: the correlation matrix between  $Z$  computed for the BC, and BC diagnostic ratios along with log of bolometric luminosity, log of black hole mass and log of Eddington ratio. Right panel: Same, but for the BLUE component. The numbers in each square show the Spearman rank correlation coefficient. The color hue is proportional to the correlation, from dark blue (strong negative correlation) to red (strong positive correlation).

low  $L/L_{\text{Edd}}$  of Sample 3 (based on  $M_{\text{BH}}$  estimates from AlIII of Marziani & Sulentic (2014)). The small dispersion in physical properties of the present sample (0.2 dex) focuses the analysis on properties that may differ for fixed accretion parameters, and fixed ratio of radiation and gravitation forces.

### 5.2.1. Correlation between diagnostic ratios and AGN physical properties

Considering the small dispersion in  $M_{\text{BH}}$ ,  $L/L_{\text{Edd}}$  and bolometric luminosity, it is hardly surprising that none of the ratios utilized in this paper is significantly correlated with the accretion parameter. The highest degree of correlation is seen between  $L/L_{\text{Edd}}$  and CIV/AlIII, but still below the minimum  $\rho$  needed for a statistically significant correlation.

In Figure 14 we present the correlation between metallicity and diagnostic ratios along with log of bolometric luminosity, log of black hole mass and log of Eddington ratio for BC and BLUE. The strongest correlation between  $Z_{\text{BC}}$  and intensity ratios are with SiIV/HeII $\lambda$ 1640 (0.81) and AlIII/HeII $\lambda$ 1640 (0.76). For  $Z_{\text{BLUE}}$ , SiIV/HeII $\lambda$ 1640 (BLUE components) correlates strongly (0.74).  $Z_{\text{BLUE}}$  correlates with physical parameters, whereas  $Z_{\text{BC}}$  rather anti-correlates with them but not at a statistically significant level. Considering the limited range in luminosity and  $M_{\text{BH}}$ , and small sample size, these trends should be confirmed.

The metallicity values we derive are very high among quasars analyzed with similar techniques (e.g., Nagao et al. 2006b; Shin et al. 2013; Sulentic et al. 2014): as

mentioned, typical values for high- $z$  quasars are around  $5Z_{\odot}$ . This value could be taken as a reference over a broad range of redshift, and also for the sample considered in the present paper, as there is no evidence of metallicity evolution in the BLR up to  $z \approx 7.5$  (e.g., Nagao et al. 2006b; Juarez et al. 2009; Xu et al. 2012; Onoue et al. 2020). This is in line with the results of Negrete et al. (2012) who found very similar intensity ratios for the prototypical NLSy1 and xA source I Zw 1, of relatively low luminosity at low  $z$ , and a luminous xA object at redshift  $z \approx 3.23$ . Even if these authors did not derive  $Z$  from their data, the I Zw 1 intensity ratios reported in their paper indicate very high metallicity consistent with the values derived for the present sample.

More than inferences on the global enhancement of  $Z$  in the host galaxies, the absence of evolution points toward a circumnuclear source of metal enrichment, ultimately associated with a Starburst (e.g., Collin & Zahn 1999a; Xu et al. 2012).

A detailed comparison with previous work on the dependence of  $Z$  on accretion parameters is hampered by two difficulties. (1) Before comparing the intensity ratios of this paper, we should consider that other authors do not distinguish between BLUE and BC when computing the ratios. This has the unfortunate implications that in some cases such as AlIII/CIV, the ratio is taken between lines emitted predominantly in different regions (virialized and wind), presumably in very different physical conditions. Not distinguishing between BC and BLUE yields CIV/AlIII  $\sim 10 \gg 1$ . (2) Methods of  $M_{\text{BH}}$  estimate differ. For example Matsuoka et al. (2011) use the Vestergaard & Peterson (2006) scaling laws without any correction to the line width of CIV. This might easily imply overestimates of the  $M_{\text{BH}}$  by factor 5 – 10 (Sulentic et al. 2007). More properly, the analysis by Shemmer et al. (2004) used H $\beta$  from optical and IR observations to compute  $M_{\text{BH}}$  and to examine the dependence of metallicity on accretion parameters. These authors found the strongest dependence on Eddington ratio (with respect to luminosity and mass) over 6 orders of magnitude in luminosity, suggesting that luminosity and black hole mass are by far less relevant (as also found, for example, by Shin et al. 2013).

### 5.3. A posteriori analysis of NV strength

As it was stressed in several works (e.g. Wang et al. 2012a; Sulentic et al. 2014, the intensity of the NV line is difficult to estimate due to blending with Ly $\alpha$  and strongly affected by absorption. We model Ly $\alpha$  and NV using the same criteria as in SiIV modelling. However, in this work, we give only a qualitative judgement of NV



strength for our sample, because of large uncertainties due to effect mentioned above. For sources in the highest metallicity range obtained from ratios from BC, the NV broad component intensity is slightly higher or comparable to Ly $\alpha$  broad component. Blue components dominate both lines. We notice also significantly higher intensity of blue component in comparison to broad one in SiIV and CIV blends. An example of source of this type is shown in the upper half Fig. 15. On the contrary, sources with the lowest metallicities obtained from BC intensity ratios show the Ly $\alpha$  BC intensity higher than in NV and the BC is stronger than BLUE. The same behaviour of strong broad component we see in the SiIV and CIV ranges. An example of sources of this type is shown in the lower panels of Fig. 15. Shin et al. (2013) compared SiIV+OIV] and NV fluxes and found strong, significant correlation between them ( $\rho = 0.75$ ). The NV over HeII $\lambda$ 1640 or H $\beta$  should be a strong tracer of  $Z$ , as it is sensitive to secondary  $Z$  production and hence proportional to  $Z^2$  (Hamann & Ferland 1999). Therefore, we conclude that the NV emission is extremely strong, and consistent with very high metal content. A much more thorough investigation of the quasar absorption / emission system is needed to include NV as a  $Z$  estimator. This is deferred to further work.

#### 5.4. Role of column density

The column density assumed in the present paper is  $\log N_c = 23$  [cm $^{-2}$ ]. With this value the emitting clouds in the low-ionization conditions remain optically thick to the Lyman continuum for most of the geometrical depth of the cloud. Even if the value  $\log N_c = 23$  may appear as a lower limit for the low-ionization BLR, as higher values are required to explain low-ionization emission such as CaII and FeII (Panda 2020; Panda et al. 2020a), the emission of the intermediate and high-ionized region is confined within the fully ionized part of the line emitting gas whose extension is already much less than the geometrical depth of the gas slab for  $\log N_c = 23$ . Therefore, we expect no or negligible effect from an increase in the column density for the low ionization part of the BLR.

For BLUE, the situation is radically different, and we have no actual strong constraints on column density. Most emission may come from a clumpy outflow (Matthews 2016, and references therein), and therefore assuming a constant  $N_c$  may not be appropriate. Considering the poor constrain that we are able to obtain, we leave the issue to an eventual investigation.

#### 5.5. Role of turbulence

The results presented in this work refer to the case in which there is no significant micro turbulence included

in the CLOUDY computations. Fig. 16 shows that at low ionization the effect is relatively modest, and that in the high-ionization case appropriate for BLUE the effect is very modest. Less obvious is the behavior at low-ionization for  $R_{\text{FeII}}$ : it shows an increase for  $t = 10$  km s $^{-1}$ , but then it has a surprising drop at larger value of the micro-turbulence. While the increase can be explained by an increase of the transitions for which fluorescence is possible, the decrease is not of obvious interpretation. It has been however confirmed by the independent set of simulation of Panda et al. (2018, 2019) who used the more recent version of CLOUDY C17.01 (Ferland et al. 2017).

#### 5.6. Metal segregation?

Metals are expected to be preferentially accelerated by resonance scattering (e.g., Proga 2007b; Risaliti & Elvis 2010). In principle, for a sufficiently large photon flux, the acceleration of metals by radiation pressure might become larger than the Coulomb friction, therefore causing a decoupling of the metals with respect to their parent plasma (Baskin & Laor 2012). This possibility has been explored in the context of the BALs, and broad absorption and emission components are expected to be related (Elvis 2000; Xu et al. 2020). The ionization parameter values are however several orders of magnitudes higher than the ones derived for the BLUE emission component. In addition our  $Z$  estimates for the BLUE suggest, if anything, values lower or equal than for the BC, whose  $Z$  might be related more to the original chemical composition of the gas in the accretion material. However, we ascribe the systematic differences between BC and BLUE as uncertainties in the method and measurement, so that  $Z$  from BLUE and BC should be considered intrinsically equal.

Considering that the most metal rich stars, galaxies, and molecular clouds in the Universe do not exceed  $Z \approx 5Z_\odot$  (Maiolino & Mannucci 2019), circumnuclear star formation is needed for the chemical enrichment of the BLR gas (e.g., Collin & Zahn 1999a,b; Wang et al. 2011, 2012b). Star formation may occur in the self gravitating, outer part of the disk. An alternative possibility is that a massive star could be formed inside the disk by accretion of disk gas (Cantiello et al. 2020).

##### 5.6.1. Abundance pollution?

An implication of the scenarios involving circumnuclear or even nuclear star formation is that there could be an alteration of the relative abundance of elements with respect to the standard solar composition (Anders & Grevesse 1989; Grevesse & Sauval 1998). Some support is provided by the extreme CIV/SiIV and CIV/AlIII

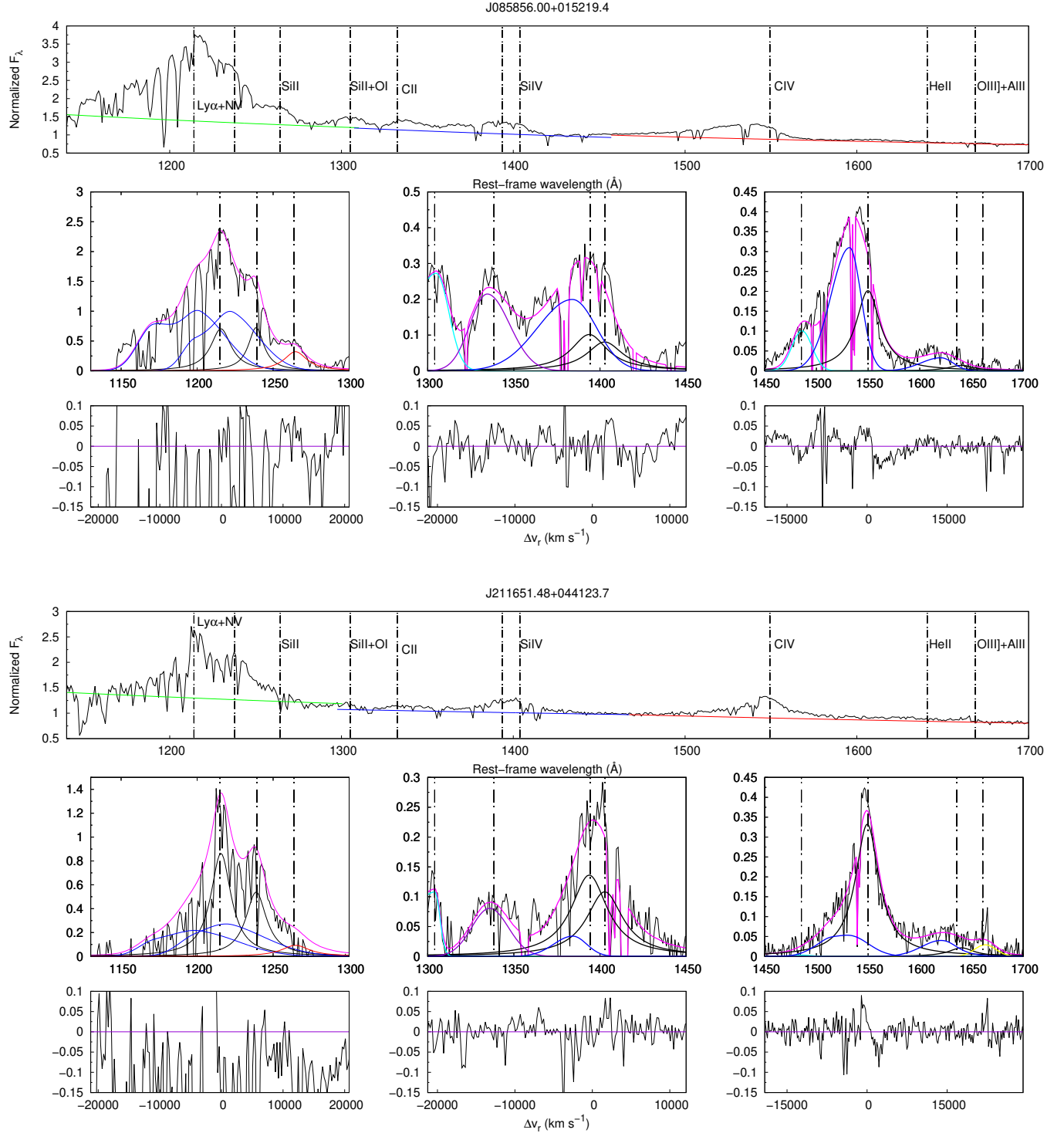


**Figure 15.** Analysis of sources showing the  $\text{Ly}\alpha + \text{Nv}$  blend. Top: calibrated rest-frame spectrum of SDSS J085856.00+015219.4. before continuum subtraction. Global or local continuum are specified by a continuous coloured line, while the black line mark rest-framed data. Dot-dashed vertical lines correspond to the rest-frame wavelength of each emission line. Bottom: multicomponent fits after continuum subtraction for the  $\text{Ly}\alpha\lambda 1216$ ,  $\text{SiIV}\lambda 1397$  and  $\text{CIV}\lambda 1549$  spectral ranges. The continuous black line marks the broad component at rest-frame associated to  $\text{Ly}\alpha\lambda 1216$ ,  $\text{NV}\lambda 1240$ ,  $\text{SiIV}\lambda 1397$  and  $\text{CIV}\lambda 1549$ . The blue one marks the blueshifted component associated to each emission. The magenta line correspond to the fit to the whole spectrum. In the left bottom panel, the red line corresponds to  $\text{SiII}\lambda 1265$ . In the middle bottom panel, the light blue line marks the contribution of  $\text{OI} + \text{SiII}\lambda 1304$  blend, while the violet line corresponds to the  $\text{CII}\lambda 1335$  emission line. In the  $\text{CIV}\lambda 1549$  region,  $\text{NIV}\lambda 1486$  is represented by a light blue line, while the gold one corresponds to the  $\text{OIII}\lambda 1663 + \text{AIII}\lambda 1670$  blend. Lower panels correspond to the residuals, in radial velocity units  $\text{km s}^{-1}$  and in Å. Bottom: Same as in the previous panels, for SDSS J211651.48+044123.7.

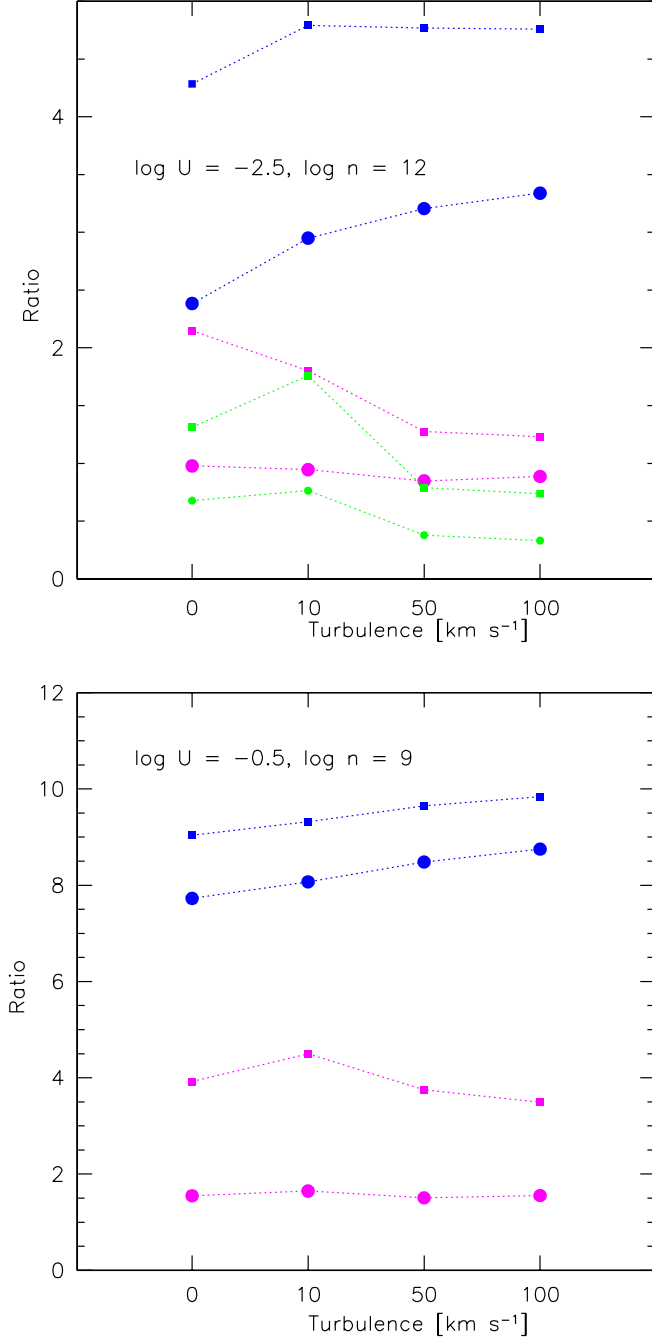


**Figure 16.** Effects of turbulence on diagnostic line ratios, for  $\text{CIV}/\text{HeII}\lambda 1640$  (blue) and  $\text{SiIV}/\text{HeII}\lambda 1640$  (magenta), considering 5 (circles) and 20  $Z_{\odot}$  (squares). The top panel assumes the low ionization conditions appropriate for BC emission, the bottom one for BLUE. In the top panel the green lines trace the same trends for the FeII blend at  $\lambda 4570$  over  $\text{H}\beta$  ratio i.e.,  $R_{\text{FeII}}$ .

that may hint to a selective enhancement of Al with respect to C. As suggested by Negrete et al. (2012), core-collapse supernovae with very massive progenitors could be at the origin of a selective enhancement. Supernovae with progenitors of masses between 15 and 40  $M_{\odot}$  have selective enhancement in their yields of Al and Si by factors of  $\approx 100$  and 10 relative to hydrogen with respect to solar (Chieffi & Limongi 2013). Since Carbon is also increased by a factor  $\sim 10$  with respect to solar, the  $[\text{Al}/\text{C}]$  is expected to be a factor  $\sim 10$  the solar value in supernova ejecta. The case for Silicon is less clear, as the enhancement is of the same order of magnitude of the one expected for Carbon. Pollution of gas by supernovae may therefore lead to an estimate of the  $Z$  higher than the actual one, if solar relative abundances are assumed. This possibility will be explored in an eventual work (Garnica et al., in preparation).

### 5.7. Implications for quasar structure evolution

Metallicity and the outflow prominence of quasars were found to be highly correlated (Wang et al. 2012a; Shin et al. 2017). The implication of these results is that xA sources, which show the highest blueshifts (Sulentic et al. 2017; Vietri et al. 2018; Martínez-Aldama et al. 2018; Martínez-Aldama et al. 2018), should also be the most metal rich. The xA sources should be at the top of the  $Z$  outflow parameter correlation of Wang et al. (2012a), if  $Z \gtrsim 10Z_{\odot}$ .

There is evidence of a metallicity correlation between BLR and NLR (Du et al. 2014), as expected if the outflows on spatial scales of kpc are originating in a disk wind. Zamanov et al. (2002) derived very small spatial scales at low luminosity. This provides additional support to the idea that xA sources – which at low- $z$  phenomenologically appear as FeII-strong NLSy1s, are relatively young sources. Their low  $[\text{OIII}]\lambda 5007$  equivalent width implied young age more than orientation effects (Risaliti et al. 2011; Bisogni et al. 2017). The  $z \approx 2$  quasars of the present sample are radiating at relatively high  $L/L_{\text{Edd}}$  although there are no examples of the extremes of xA sources showing blueshifted emission in AlIII as prominent as the one of CIV (e.g., Martínez-Aldama et al. 2017). There is no evidence of heavy obscuration. They are certainly out of the obscured early evolution stage in which the accreting black hole is enveloped by gas and dust (see the sketch in D’Onofrio & Marziani 2018). The  $W$  CIV distribution covers the upper half of the one of Martínez-Aldama et al. (2018). There are no weak-lined quasars following Diamond-Stanic et al. (2009). The xA sources of the present sample may have reached a sort of stable equilibrium between gravitation and radiation forces

made perhaps possible by the development by an optically thick, geometrically thick accretion disk, and by its anisotropic radiation properties (e.g., Abramowicz et al. 1988; Szuszkiewicz et al. 1996; Sądowski et al. 2014).

The median value of the peak displacement of the BLUE component is around  $\approx 3500 \text{ km s}^{-1}$ , and the centroid at half maximum is shifted by  $5000 \text{ km s}^{-1}$ . The extreme blueshifts in the metal lines imply outflows that may not remain bound to the potential well of the black hole and of the inner bulge of the host galaxies (e.g., Marziani et al. 2016b, and references therein). The high metal content of the outflows, estimated by the present work to be in the range  $10 - 100Z_{\odot}$ , implies that these sources are likely to be a major source of metal enrichment of the interstellar gas of the host galaxy and of the intergalactic medium. Using a standard estimate for the mass outflow rate  $\dot{M}$  (Marziani et al. 2016b),  $\dot{M} \approx 15L_{\text{CIV},45}v_{5000}r_{1\text{pc}}^{-1}n_9^{-1}M_{\odot} \text{ yr}^{-1}$ , we obtain an outflow rate of  $\dot{M} \approx 20M_{\odot} \text{ yr}^{-1}$ , assuming median values for the sources of our sample: median outflow velocity from the peak of BLUE  $\approx -3500 \text{ km s}^{-1}$ , a median luminosity of the CIV BLUE (corrected because of Galactic extinction) of  $4.2 \cdot 10^{44} \text{ erg s}^{-1}$ , a median radius  $5.9 \cdot 10^{17} \text{ cm}$  from the Kaspi et al. (2007) radius-luminosity correlation for CIV, and  $n_9 = 1$ . For a duty cycle of  $\sim 10^8 \text{ yr}$ , the expelled mass of heavily enriched-gas could be  $\sim 10^9 M_{\odot}$ .

## 6. CONCLUSION

The sources at the extreme end of Population A along the main sequence are defined by the prominence of their FeII emission and, precisely, by the selection criterion  $R_{\text{FeII}} \gtrsim 1$  (Marziani & Sulentic 2014; Du et al. 2016b). Their properties as a class are scarcely known. Even if there has been a long history of studies focused on FeII-strong sources since Lipari et al. (1993); Graham et al. (1996), their relevance to galactic and large scale structure evolution is being reconsidered anew with the help of the quasar main sequence. This paper adds to other aspects that were considered by previous investigations (for example, the very powerful outflows, the disjoint low- and high-ionization emitting regions, first suggested by Collin-Souffrin et al. 1988), a quantitative analysis of the chemical composition of xA sources. The main aspects of the present investigations can be summarized as follows:

- We distinguish between two emission line components most likely origination from emitting in widely different physical conditions: a virialized low-ionization BLR, and a high-ionization region associated to a very strong blueshifted excess in

the CIV emission line. This is the *conditio sine qua non* for meaningful  $Z$  estimates.

- The physical conditions in the low and high regions were confirmed to be very different, with the low ionization ( $U, n_{\text{H}} \approx (-2.75, 13)$ ) and the high ionization ( $U, n_{\text{H}} \approx (-0.5, 8 - 9)$ ). The high ionization region parameters are however poorly constrained.
- Using intensity ratios between the strongest metal lines and HeII $\lambda 1640$  emission at  $\lambda 1640$  we derive metallicity values in the range  $10 \lesssim Z \lesssim 100Z_{\odot}$ , with most likely values around several tens of the time solar metallicity.
- We find evidence of overabundance of Al with respect to C. This result points toward possible pollution of the broad line emitting gas chemical composition by supernova ejecta.

xA quasars are perhaps the only quasars whose ejection are able to overcome the potential well of the black hole and of the host galaxy. Applying the method to large samples of quasars would permit to constrain the metal enrichment processes on a galactic scale.

The present analysis relied heavily on the HeII $\lambda 1640$  line which is of low equivalent width and with a flat, very broad profile (incidentally, we note that the low equivalent width is consistent the high  $Z$  of the emitting regions). Therefore, a more precise analysis would require spectra of moderate dispersion but of higher S/N ratio. A large part of the scatter and/or systematic difference for various  $Z$  estimators is related to difficulty to isolate faint and broad emission in relatively noisy spectra.

## ACKNOWLEDGMENTS

MS acknowledges the support of the Erasmus+ programme of the European Union and would like express my very great appreciation to Istituto Nazionale di Astrofisica (INAF) Osservatorio Astronomico di Padova, University of Padova and Astronomical Observatory of the University of Warsaw for enabling to complete an internship. The project was partially supported by the Polish Funding Agency National Science Centre project 2017/26/A/ST9/00756 (MAESTRO 9) and MNiSW grant DIR/WK/2018/12. PM acknowledges the Hypatia of Alexandria visiting grant SO-IAA (SEV-2017-0709) through the Center of Excellence Severo Ochoa, and is deeply indebted to Drs. J. Perea and A. del Olmo for the generous allocation of computing resources and for a stay at IAA. AdO acknowledges financial support from the Spanish grants MCI PID2019-106027GB-C41 and the State Agency for Research of the Spanish MCIU through the Center of Excellence Severo Ochoa award for the Instituto de Astrofísica de Andalucía (SEV-2017-0709).

Funding for the Sloan Digital Sky Survey (SDSS) has been provided by the Alfred P. Sloan Foundation, the

Participating Institutions, the National Aeronautics and Space Administration, the National Science Foundation, the U.S. Department of Energy, the Japanese Monbukagakusho, and the Max Planck Society. The SDSS Web site is <http://www.sdss.org/>.

The SDSS is managed by the Astrophysical Research Consortium (ARC) for the Participating Institutions. The Participating Institutions are The University of Chicago, Fermilab, the Institute for Advanced Study, the Japan Participation Group, The Johns Hopkins University, Los Alamos National Laboratory, the Max-Planck-Institute for Astronomy (MPIA), the Max-Planck-Institute for Astrophysics (MPA), New Mexico State University, University of Pittsburgh, Princeton University, the United States Naval Observatory, and the University of Washington.

## REFERENCES

- Abramowicz, M. A., Czerny, B., Lasota, J. P., & Szuszkiewicz, E. 1988, *ApJ*, 332, 646
- Adelman-McCarthy, J. K., Agüeros, M. A., Allam, S. S., et al. 2008a, *ApJS*, 175, 297
- . 2008b, *ApJS*, 175, 297
- Adhikari, T. P., Róžańska, A., Czerny, B., Hryniewicz, K., & Ferland, G. J. 2016, *ApJ*, 831, 68
- Anders, E., & Grevesse, N. 1989, *GeoCoA*, 53, 197
- Bañados, E., Venemans, B. P., Decarli, R., et al. 2016, *ApJS*, 227, 11
- Baldwin, J. A., Hamann, F., Korista, K. T., et al. 2003, *ApJ*, 583, 649
- Baskin, A., & Laor, A. 2012, *MNRAS*, 426, 1144
- Becker, R. H., White, R. L., & Helfand, D. J. 1995, *ApJ*, 450, 559
- Bisogni, S., di Serego Alighieri, S., Goldoni, P., et al. 2017, *A&A*, 603, A1
- Boroson, T. A., & Green, R. F. 1992, *ApJS*, 80, 109
- Brotherton, M. S., Wills, B. J., Francis, P. J., & Steidel, C. C. 1994, *ApJ*, 430, 495
- Brühweiler, F., & Verner, E. 2008, *ApJ*, 675, 83
- Cantiello, M., Jermyn, A. S., & Lin, D. N. C. 2020, *arXiv e-prints*, [arXiv:2009.03936](https://arxiv.org/abs/2009.03936)
- Chieffi, A., & Limongi, M. 2013, *ApJ*, 764, 21
- Coatman, L., Hewett, P. C., Banerji, M., & Richards, G. T. 2016, *MNRAS*, 461, 647
- Collin, S., & Zahn, J.-P. 1999a, *A&Ap*, 344, 433
- . 1999b, *Ap&SS*, 265, 501
- Collin-Souffrin, S., Dyson, J. E., McDowell, J. C., & Perry, J. J. 1988, *MNRAS*, 232, 539
- Collin-Souffrin, S., & Lasota, J.-P. 1988, *PASP*, 100, 1041
- Corbin, M. R., & Boroson, T. A. 1996, *ApJS*, 107, 69
- D’Agostini, G. 2003, *Bayesian reasoning in data analysis - A critical introduction* (Singapore: World Scientific Co.)
- Davidson, K., & Netzer, H. 1979, *Reviews of Modern Physics*, 51, 715
- Diamond-Stanic, A. M., Fan, X., Brandt, W. N., et al. 2009, *ApJ*, 699, 782
- Dietrich, M., Hamann, F., Shields, J. C., et al. 2003, *ApJ*, 589, 722
- D’Onofrio, M., & Marziani, P. 2018, *Frontiers in Astronomy and Space Sciences*, 5, 31
- Du, P., Wang, J.-M., Hu, C., et al. 2016a, *ApJL*, 818, L14
- . 2014, *MNRAS*, 438, 2828
- Du, P., Lu, K.-X., Hu, C., et al. 2016b, *ApJ*, 820, 27
- Elvis, M. 2000, *ApJ*, 545, 63
- Feibelman, W. A., & Aller, L. H. 1987, *ApJ*, 319, 407



- Ferland, G. J., Done, C., Jin, C., Landt, H., & Ward, M. J. 2020, *MNRAS*, 494, 5917
- Ferland, G. J., Hu, C., Wang, J., et al. 2009, *ApJL*, 707, L82
- Ferland, G. J., Porter, R. L., van Hoof, P. A. M., et al. 2013, *RevMexA&Ap*, 49, 137
- Ferland, G. J., Chatzikos, M., Guzmán, F., et al. 2017, *RMxAA*, 53, 385
- Gaskell, C. M. 2000, *NewAR*, 44, 563
- Graham, M. J., Clowes, R. G., & Campusano, L. E. 1996, *MNRAS*, 279, 1349
- Grevesse, N., & Sauval, A. J. 1998, *SSRv*, 85, 161
- Hamann, F., & Ferland, G. 1992, *ApJL*, 391, L53
- . 1999, *ARA&A*, 37, 487
- Hamann, F., Korista, K. T., Ferland, G. J., Warner, C., & Baldwin, J. 2002, *ApJ*, 564, 592
- Hartig, G. F., & Baldwin, J. A. 1986, *ApJ*, 302, 64
- Izotov, Y. I., & Thuan, T. X. 1999, *ApJ*, 511, 639
- Juarez, Y., Maiolino, R., Mujica, R., et al. 2009, *A&Ap*, 494, L25
- Kaspi, S., Brandt, W. N., Maoz, D., et al. 2007, *ApJ*, 659, 997
- Keenan, F. P., Ahmed, S., Brage, T., et al. 2002, *MNRAS*, 337, 901
- Kovačević-Dojčinović, J., & Popović, L. Č. 2015, *ApJS*, 221, 35
- Kriss, G. 1994, *Astronomical Data Analysis Software and Systems III*, A.S.P. Conference Series, 61, 437
- Kuraszkiewicz, J., Wilkes, B. J., Schmidt, G., et al. 2009, *ApJ*, 692, 1180
- Leighly, K. M., & Moore, J. R. 2004, *ApJ*, 611, 107
- Lipari, S., Terlevich, R., & Macchetto, F. 1993, *ApJ*, 406, 451
- Maiolino, R., & Mannucci, F. 2019, *A&A Rv*, 27, 3
- Martínez-Aldama, M. L., Del Olmo, A., Marziani, P., et al. 2017, *Frontiers in Astronomy and Space Sciences*, 4, 29
- Martínez-Aldama, M. L., del Olmo, A., Marziani, P., et al. 2018, *A&A*, 618, A179
- Martínez-Aldama, M. L., Del Olmo, A., Marziani, P., et al. 2018, *Frontiers in Astronomy and Space Sciences*, 4, 65
- Marziani, P., Martínez Carballo, M. A., Sulentic, J. W., et al. 2016a, *Ap&SS*, 361, 29
- Marziani, P., & Sulentic, J. W. 2014, *MNRAS*, 442, 1211
- Marziani, P., Sulentic, J. W., Dultzin-Hacyan, D., Calvani, M., & Moles, M. 1996, *ApJS*, 104, 37
- Marziani, P., Sulentic, J. W., Negrete, C. A., et al. 2010, *MNRAS*, 409, 1033
- Marziani, P., Sulentic, J. W., Stirpe, G. M., et al. 2016b, *Ap&SS*, 361, 3
- Marziani, P., Sulentic, J. W., Stirpe, G. M., Zamfir, S., & Calvani, M. 2009, *A&Ap*, 495, 83
- Marziani, P., Dultzin, D., Sulentic, J. W., et al. 2018, *Frontiers in Astronomy and Space Sciences*, 5, 6
- Mathews, W. G., & Ferland, G. J. 1987, *ApJ*, 323, 456
- Mathur, S. 2000, *MNRAS*, 314, L17
- Matsuoka, K., Nagao, T., Marconi, A., Maiolino, R., & Taniguchi, Y. 2011, *A&A*, 527, A100
- Matsuoka, Y., Oyabu, S., Tsuzuki, Y., & Kawara, K. 2007, *ApJ*, 663, 781
- Matthews, J. H. 2016, PhD thesis, University of Southampton
- Mejía-Restrepo, J. E., Trakhtenbrot, B., Lira, P., Netzer, H., & Capellupo, D. M. 2016, *MNRAS*, 460, arXiv:1603.03437
- Murray, N., & Chiang, J. 1997, *ApJ*, 474, 91
- Murray, N., Chiang, J., Grossman, S. A., & Voit, G. M. 1995, *ApJ*, 451, 498
- Nagao, T., Maiolino, R., & Marconi, A. 2006a, *A&A*, 447, 863
- Nagao, T., Marconi, A., & Maiolino, R. 2006b, *A&Ap*, 447, 157
- Nardini, E., Lusso, E., Risaliti, G., et al. 2019, *A&A*, 632, A109
- Negrete, A., Dultzin, D., Marziani, P., & Sulentic, J. 2012, *ApJ*, 757, 62
- Negrete, C. A., Dultzin, D., Marziani, P., & Sulentic, J. 2010, *ArXiv e-prints*, arXiv:1011.4248
- Negrete, C. A., Dultzin, D., Marziani, P., & Sulentic, J. W. 2014, *ApJ*, 794, 95
- Negrete, C. A., Dultzin, D., Marziani, P., et al. 2018, *A&A*, 620, A118
- Netzer, H., & Marziani, P. 2010, *ApJ*, 724, 318
- Onoue, M., Bañados, E., Mazzucchelli, C., et al. 2020, *ApJ*, 898, 105
- Osmer, P. S., & Smith, M. G. 1976, *ApJ*, 210, 267
- Osterbrock, D. E., & Ferland, G. J. 2006, *Astrophysics of gaseous nebulae and active galactic nuclei* (Mill Valley, CA: University Science Books)
- Osterbrock, D. E., & Pogge, R. W. 1985, *ApJ*, 297, 166
- Panda, S. 2020, *arXiv e-prints*, arXiv:2004.13113
- Panda, S., Czerny, B., Adhikari, T. P., et al. 2018, *ApJ*, 866, 115
- Panda, S., Martínez-Aldama, M. L., Marinello, M., et al. 2020a, *arXiv e-prints*, arXiv:2004.05201
- Panda, S., Marziani, P., & Czerny, B. 2019, *ApJ*, 882, 79
- . 2020b, *Contributions of the Astronomical Observatory Skalnaté Pleso*, 50, 293
- Pâris, I., Petitjean, P., Ross, N. P., et al. 2017, *A&A*, 597, A79

- Peterson, B. M., & Wandel, A. 1999, *ApJL*, 521, L95
- Plotkin, R. M., Shemmer, O., Trakhtenbrot, B., et al. 2015, *ApJ*, 805, 123
- Popović, L. Č., Mediavilla, E. G., Kubičela, A., & Jovanović, P. 2002, *A&A*, 390, 473
- Proga, D. 2007a, *ApJ*, 661, 693
- Proga, D. 2007b, in *Astronomical Society of the Pacific Conference Series*, Vol. 373, *The Central Engine of Active Galactic Nuclei*, ed. L. C. Ho & J.-W. Wang, 267
- Punsly, B., Marziani, P., Bennert, V. N., Nagai, H., & Gurwell, M. A. 2018, *ApJ*, 869, 143
- Richards, G. T., Lacy, M., Storrie-Lombardi, L. J., et al. 2006, *ApJS*, 166, 470
- Richards, G. T., Kruczek, N. E., Gallagher, S. C., et al. 2011, *AJ*, 141, 167
- Risaliti, G., & Elvis, M. 2010, *A&A*, 516, A89
- Risaliti, G., Salvati, M., & Marconi, A. 2011, *MNRAS*, 411, 2223
- Sądowski, A., Narayan, R., McKinney, J. C., & Tchekhovskoy, A. 2014, *MNRAS*, 439, 503
- Schneider, D. P., Richards, G. T., Hall, P. B., et al. 2010, *AJ*, 139, 2360
- Shemmer, O., & Netzer, H. 2002, *ApJL*, 567, L19
- Shemmer, O., Netzer, H., Maiolino, R., et al. 2004, *ApJ*, 614, 547
- Shen, Y. 2016, *ApJ*, 817, 55
- Shen, Y., & Ho, L. C. 2014, *Nature*, 513, 210
- Shen, Y., Richards, G. T., Strauss, M. A., et al. 2011, *ApJS*, 194, 45
- Shields, G. A. 1976, *ApJ*, 204, 330
- Shin, J., Nagao, T., & Woo, J.-H. 2017, *ApJ*, 835, 24
- Shin, J., Woo, J.-H., Nagao, T., & Kim, S. C. 2013, *ApJ*, 763, 58
- Sulentic, J. W., Bachev, R., Marziani, P., Negrete, C. A., & Dultzin, D. 2007, *ApJ*, 666, 757
- Sulentic, J. W., Marziani, P., del Olmo, A., et al. 2014, *A&A*, 570, A96
- Sulentic, J. W., Marziani, P., & Dultzin-Hacyan, D. 2000a, *ARA&A*, 38, 521
- Sulentic, J. W., Marziani, P., Dultzin-Hacyan, D., Calvani, M., & Moles, M. 1995, *ApJL*, 445, L85
- Sulentic, J. W., Marziani, P., Zamanov, R., et al. 2002, *ApJL*, 566, L71
- Sulentic, J. W., Repetto, P., Stirpe, G. M., et al. 2006, *A&Ap*, 456, 929
- Sulentic, J. W., Zwitter, T., Marziani, P., & Dultzin-Hacyan, D. 2000b, *ApJL*, 536, L5
- Sulentic, J. W., del Olmo, A., Marziani, P., et al. 2017, *A&A*, 608, A122
- Szuszkievicz, E., Malkan, M. A., & Abramowicz, M. A. 1996, *ApJ*, 458, 474
- Temple, M. J., Ferland, G. J., Rankine, A. L., et al. 2020, *MNRAS*, 496, 2565
- Vanden Berk, D. E., Richards, G. T., Bauer, A., et al. 2001, *AJ*, 122, 549
- Verner, E. M., Verner, D. A., Korista, K. T., et al. 1999, *ApJS*, 120, 101
- Véron-Cetty, M.-P., Véron, P., & Gonçalves, A. C. 2001, *AAp*, 372, 730
- Vestergaard, M., & Peterson, B. M. 2006, *ApJ*, 641, 689
- Vestergaard, M., & Wilkes, B. J. 2001, *ApJS*, 134, 1
- Vietri, G., Piconcelli, E., Bischetti, M., et al. 2018, *A&A*, 617, A81
- Vila-Costas, M. B., & Edmunds, M. G. 1993, *MNRAS*, 265, 199
- Wang, H., Zhou, H., Yuan, W., & Wang, T. 2012a, *ApJL*, 751, L23
- Wang, J.-M., Du, P., Baldwin, J. A., et al. 2012b, *ApJ*, 746, 137
- Wang, J.-M., Du, P., Li, Y.-R., et al. 2014, *ApJL*, 792, L13
- Wang, J.-M., Du, P., Valls-Gabaud, D., Hu, C., & Netzer, H. 2013, *Physical Review Letters*, 110, 081301
- Wang, J.-M., Ge, J.-Q., Hu, C., et al. 2011, *ApJ*, 739, 3
- Warner, C., Hamann, F., & Dietrich, M. 2004, *ApJ*, 608, 136
- Wildy, C., Czerny, B., & Panda, S. 2019, *A&A*, 632, A41
- Wills, D., & Netzer, H. 1979, *ApJ*, 233, 1
- Xu, D., Komossa, S., Zhou, H., et al. 2012, *AJ*, 143, 83
- Xu, X., Zakamska, N. L., Arav, N., Miller, T., & Benn, C. 2020, *MNRAS*, 495, 305
- Zamanov, R., Marziani, P., Sulentic, J. W., et al. 2002, *ApJL*, 576, L9
- Zheng, W. 1988, *Astrophysical Letters and Communications*, 27, 275
- Zhou, H., Wang, T., Yuan, W., et al. 2006, *ApJS*, 166, 128

## APPENDIX

## A. REST-FRAME SPECTRA AND FITS

The spectral analysis of the 13 objects of our sample is shown in the figures below.

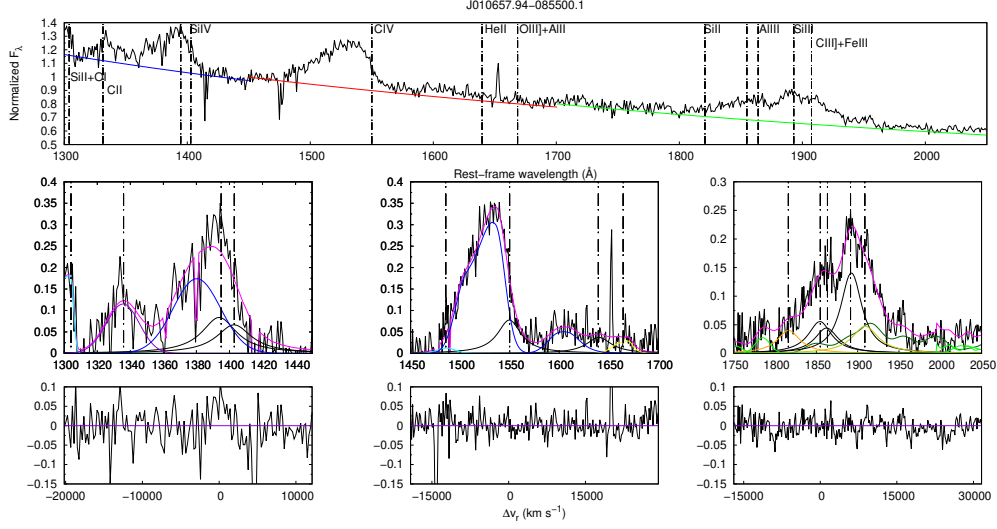


**Figure 17.** Top panels: calibrated rest-frame spectrum of SDSS J010657.94-085500.1 before continuum subtraction. Global or local continuum are specified by a continuous coloured line, while the black line mark rest-framed data. Dot-dashed vertical lines correspond to the rest-frame wavelength of each emission line. Bottom: multicomponent fits after continuum subtraction for the SiIV $\lambda$ 1397, CIV $\lambda$ 1549 and  $\lambda$ 1900 blend spectral ranges. The continuous black line marks the broad component at rest-frame associated to SiIV $\lambda$ 1397, CIV $\lambda$ 1549 and AlIII $\lambda$ 1860, the blue one marks the blueshifted component associated to each emission. The magenta line correspond to the fit to the whole spectrum. In the left bottom panel, the light blue line marks the contribution of OI + SiII $\lambda$ 1304 blend, while the violet line corresponds to the CII $\lambda$ 1335 emission line. In the CIV $\lambda$ 1549 region, NIV $\lambda$ 1486 is represented by a light blue line, while the gold one corresponds to the OIII $\lambda$ 1663 + AlIII $\lambda$ 1670 blend. In the  $\lambda$ 1900 blend range, FeIII and FeII contributions are marked dark and light green lines respectively. Violet lines mark the NIII $\lambda$ 1750, the orange one corresponds to the SiII $\lambda$ 1816 and the gold one to the CIII $\lambda$ 1909 line. Lower panels correspond to the residuals, in radial velocity units  $\text{km s}^{-1}$  and in  $\text{\AA}$ .

B. DIAGNOSTIC INTENSITY RATIOS IN THE PLANE ( $U$ ,  $n_{\text{H}}$ ) AS A FUNCTION OF METALLICITY

The results of the arrays of simulations as a function of  $n_{\text{H}}$ ,  $U$ , and  $Z$  are shown below, for  $N_{\text{c}} = 10^{23}$ . The SED shape is the same for all simulations (table\_agn) which corresponds to the SED of Mathews & Ferland (1987). No turbulence was assumed.

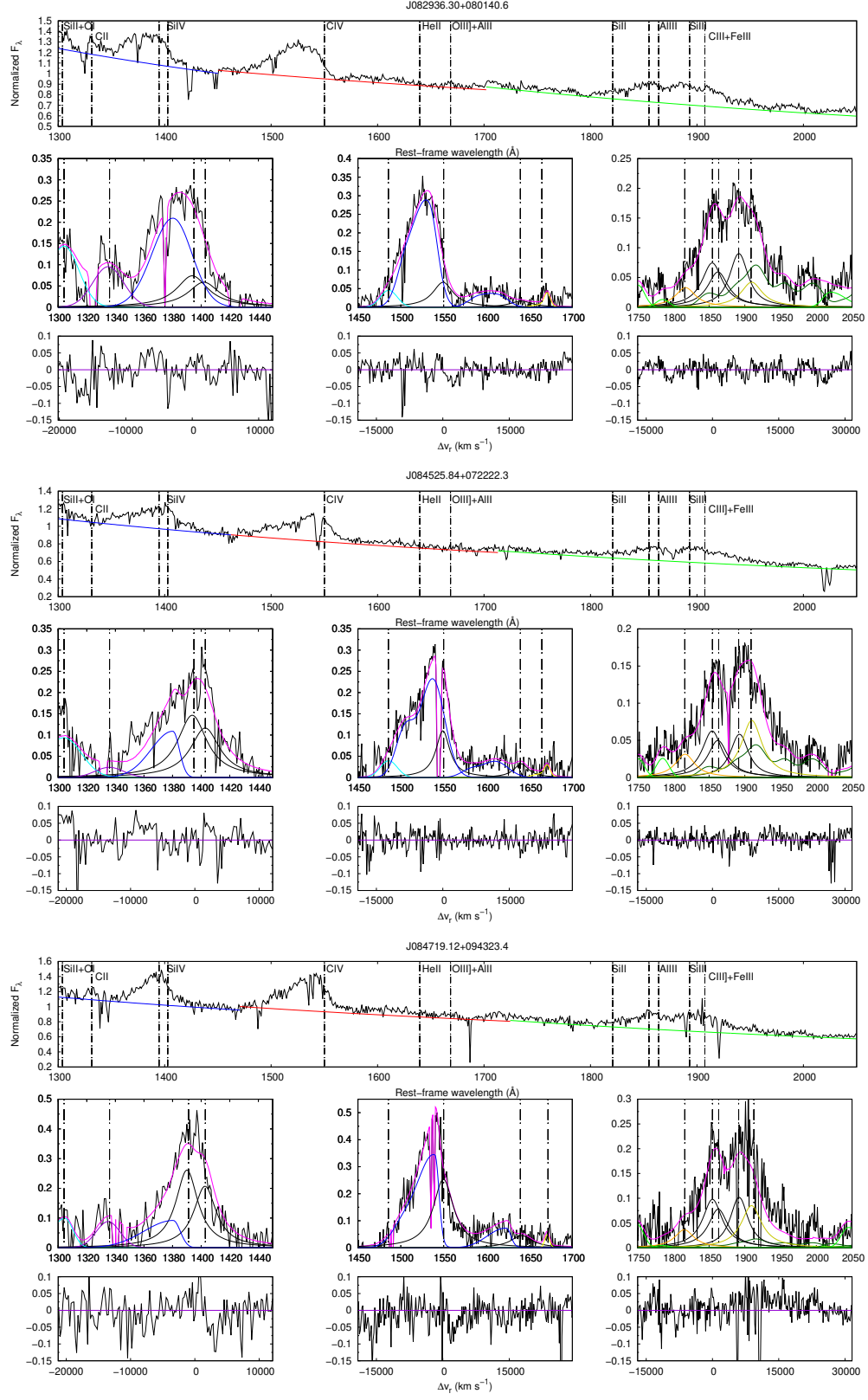


**Figure 17.** Same of the previous panel, for SDSS J082936.30+080140.6 and SDSS J084525.84+072222.3, and SDSS J084719.12+094323.4.

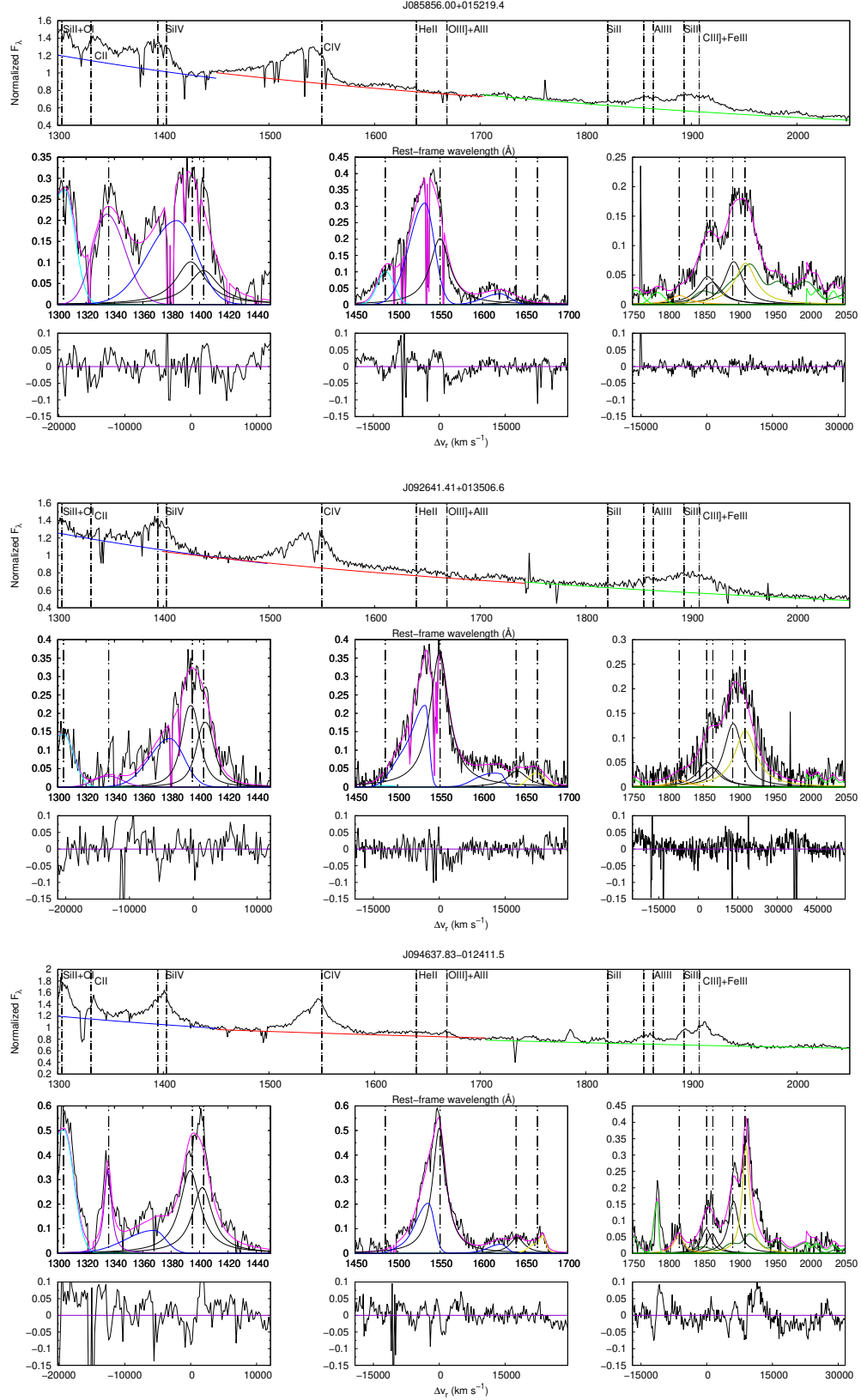


**Figure 17.** Same of the previous panel, for SDSS J085856.00+015219.4, SDSS J092641.41+013506.6, and SDSS J094637.83-012411.5.



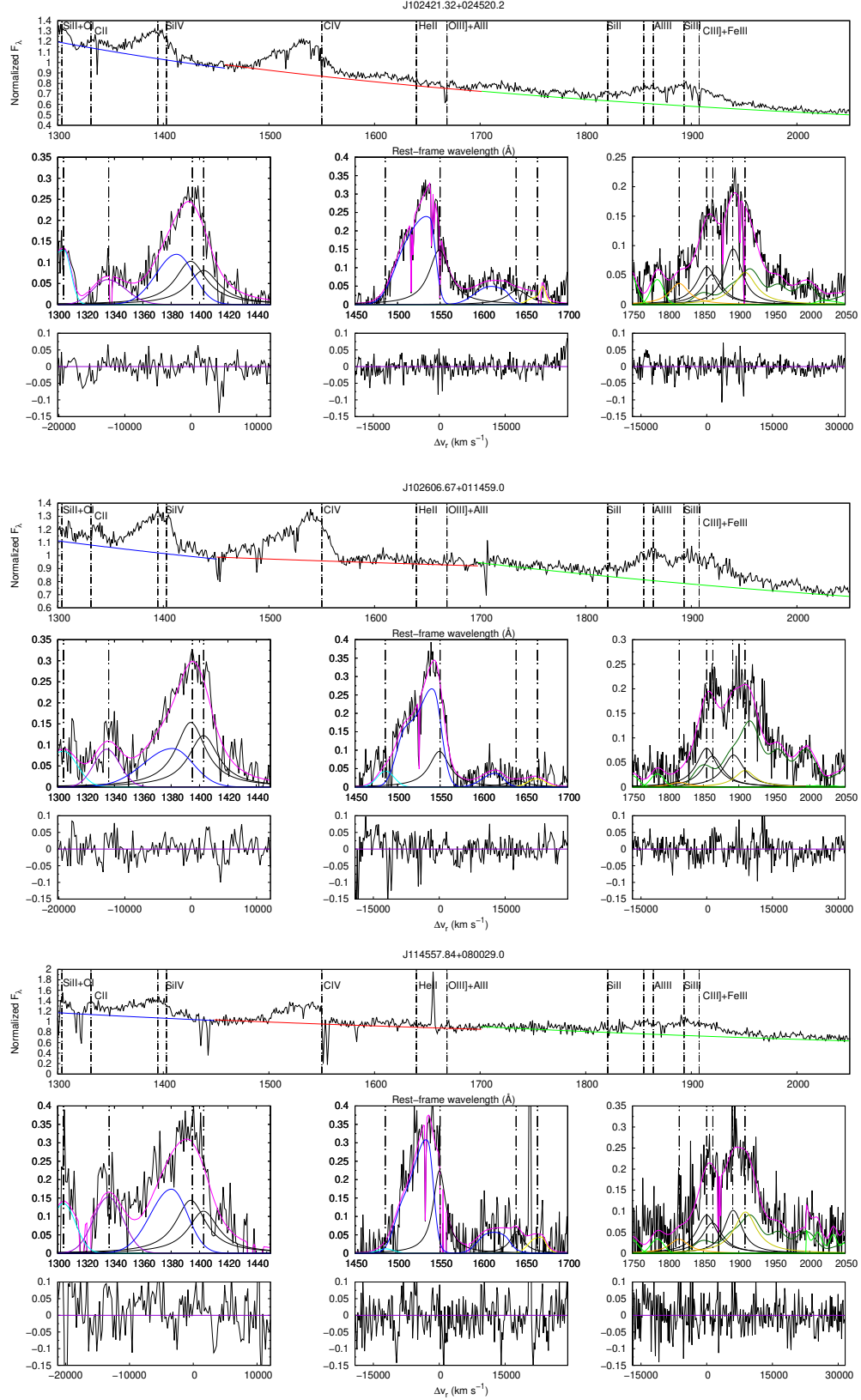


**Figure 17.** Same of the previous panel, for SDSS J102421.32+024520.2 SDSS J102606.67+011459.0 SDSS J114557.84+080029.0.

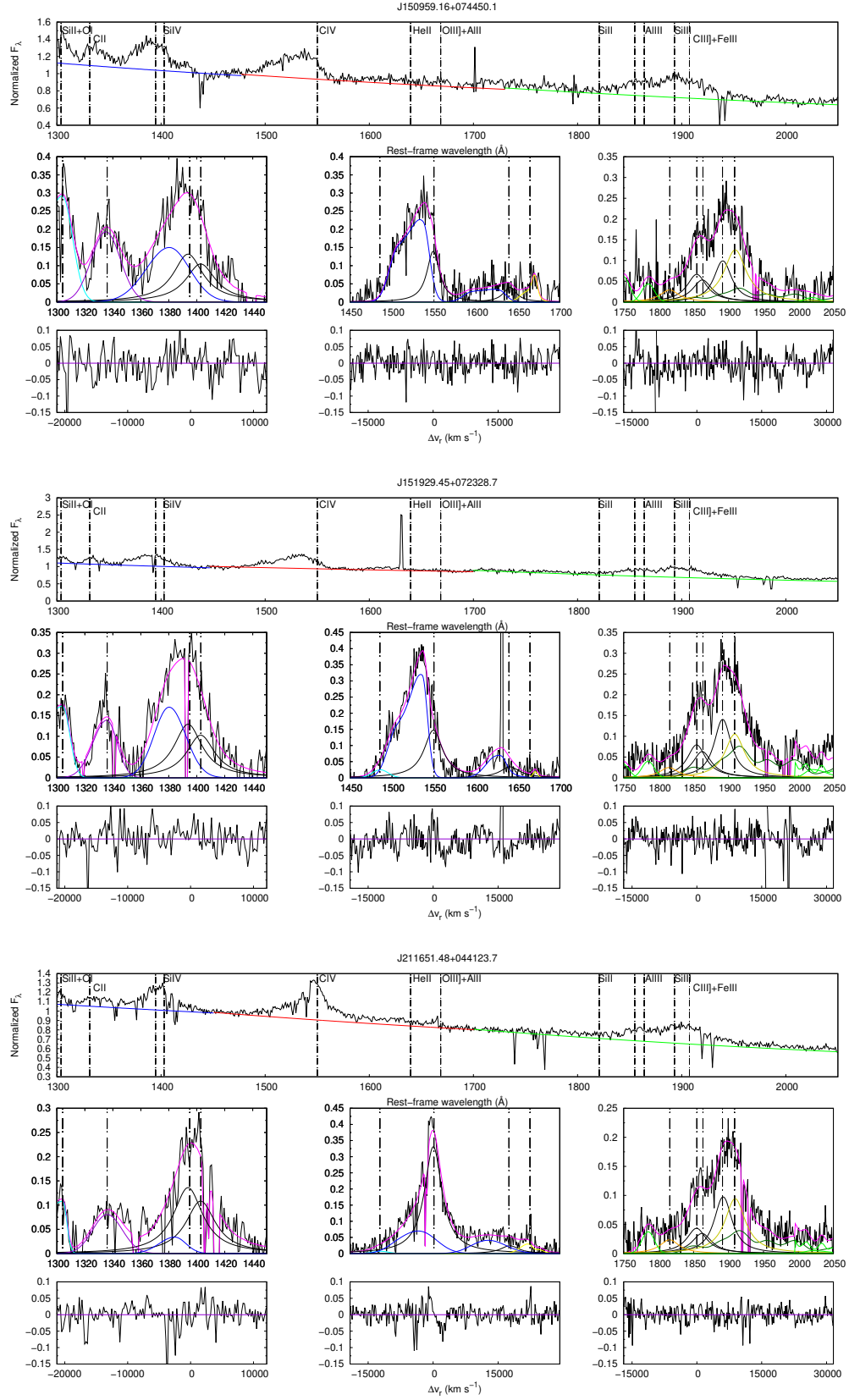


**Figure 17.** Same of the previous panel, for SDSS J150959.16+074450.1, SDSS J151929.45+072328.7, SDSS J211651.48+044123.7.

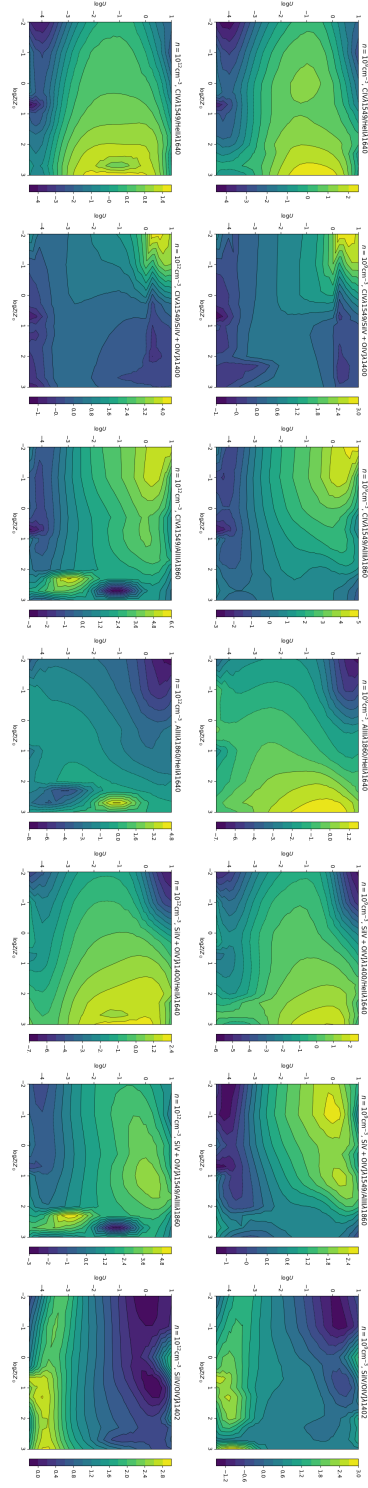


**Figure 18.** Isophotal contour in the  $\log U - \log Z$  for diagnostic line intensity ratios for  $n_{\text{H}} = 10^9 \text{ cm}^{-3}$  (top) and  $n_{\text{H}} = 10^{12} \text{ cm}^{-3}$  (bottom), for column density  $N_{\text{c}} = 10^{23} \text{ cm}^{-2}$ .

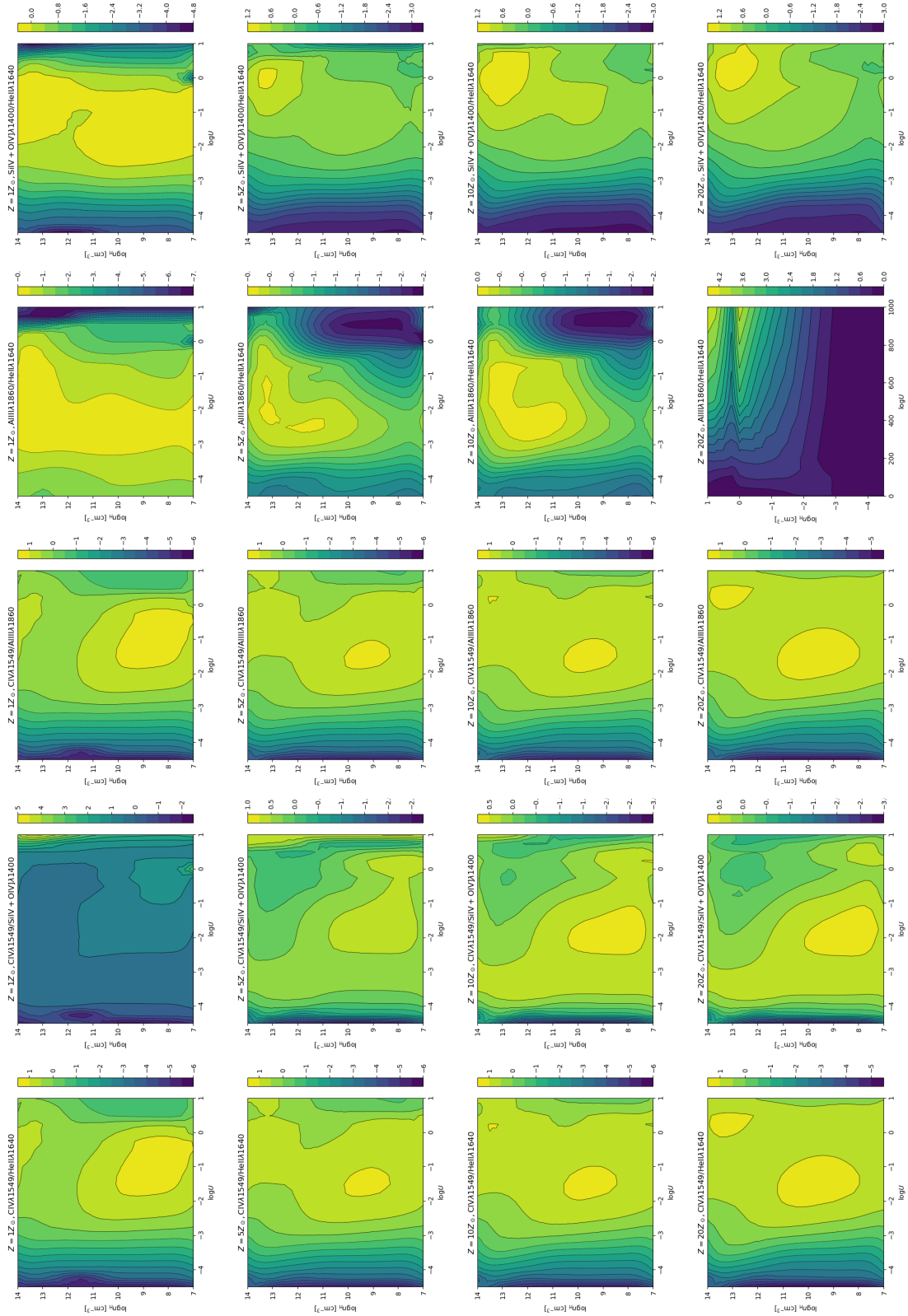


**Figure 19.** Isophotal contour in the  $\log U - \log n_H$  for line intensity ratios (from left to right) as a function of metallicity (from top-to-bottom:  $Z = 1, 5, 10, 20$ ), for column density  $N_c = 10^{23} \text{ cm}^{-2}$ .